THESIS

NON-CONJUGATE POTENTIAL-STEPPING PHENOTHIAZINE AND PHENOXAZINE BASED POLYMER HOLE-TRANSPORT MATERIAL FOR DYE-SENSITIZED SOLAR CELLS

&

INCREASING VOID SPACE IN POROUS TiO_2: TO STUDY DIFFUSION PROPERTIES OF A COBALT MEDIATOR

Submitted by

Kristoffer Persson

Department of Chemistry

In partial fulfillment of requirements

For the degree of Master of Science

Colorado State University

Fort Collins, Colorado

Fall 2012

Master's Committee:

Advisor: C. Michael Elliott

Anthony K. Rappé
Matthew J. Kipper

ABSTRACT

NON-CONJUGATE POTENTIAL STEPPING PHENOTHIAZINE AND PHENOXAZINE BASED POLYMER HOLE-TRANSPORT MATERIAL FOR DYE-SENSITIZED SOLAR CELLS

&

INCREASING VOID SPACE IN POROUS TiO_2: TO STUDY DIFFUSION PROPERTIES OF A COBALT MEDIATOR

As energy demands increase so has the search for alternative sources of energy. Although, fossil fuels have proven useful in energy production, they are also detrimental due to the negative impact on our environment. Considering the current alternative energy sources, such as wind, hydroelectric, biofuels, etc, one source of alternative energy shines above the rest, solar energy. Solar energy provides a possible solution to the energy demands of our modern world with little effect on the environment. The only waste produced from the solar cell industry is from producing and recycling the cells. After production, solar cells require no resources to function other than solar radiation, and no waste is produced. The sun has been powering life on this planet for billions of years, and bombards the earth with $3x10^{24}$ J of energy per year. Only 0.02% of this energy is currently needed to power the world, thus making the sun a viable solution to energy demands, while decreasing current pollution issues.

This thesis focuses on dye sensitized solar cell (DSSCs), in particular, the Grätzel cell, which incorporates thin films of TiO_2 as the semiconductor, DSSC's work very similarly to a battery, but instead of using chemical energy to drive electrons through the circuit, it uses

photons. Several issues have arisen with these types of solar cells and their use in the modern world. One particular problem is that the iodide/triiodide (I^-/I_3^-) mediator, which currently produces the most efficient DSSCs, is corrosive and volatile. To address this and other issues, a conductive phenothiazine (PTZ) and phenoxazine (POZ) based polymer is hypothesized to be a suitable replacement for the mediator and solvent by acting as a charge separator and hole transport material, without any volatile or corrosive problems. This polymer would hypothetically function similarly to proposed electron transport in DNA. When charges are injected into a DNA strand they are transferred through π-stacking interactions at the center of the helix, which allows electrons to tunnel through the DNA strand. A potential-stepping block co-polymer incorporating phenothiazine (PTZ) and phenoxazine (POZ) groups attached to the polymer backbone can π-stack like the base pairs in DNA. By creating a two-block co-polymer, with one composed of PTZ monomers and the other of POZ monomers, charge separation can be achieved by trapping the hole on the POZ groups due to their more negative oxidation potentials. This potential-stepping polymer charge separator is the focus of the first part of this thesis.

The second section of this thesis is centered on diffusion issues in DSSCs where the I^-/I_3^- mediator is replaced with tris((2,2'-bipyridyl-4,4'-di-*tert*-butyl)cobalt(III) perchlorate, $CoDTB^{+3}(ClO_4^-)_3$ (DTB = 4,4′-di-tert-butyl-2,2′-bipyridine). The cobalt mediator has many advantages: it is non-corrosive, non-volatile, and it is able to be tuned to optimize the electron transfer process to the dye by simple structural modifications of the ligand. However, cobalt mediators have small diffusion coefficients on the order of $1x10^{-7}$ cm^2 s^{-1} or less in TiO_2 mesoporous thin films. It has been hypothesized that changing the structure of the TiO_2 layer or increasing the void space in the films in the correct manner may dramatically increase the effective rate of diffusion. The introduction of appropriate void space will hypothetically create

channels and allow faster diffusion of the mediator. The second half of this thesis explores the effects of introducing void space into TiO_2 thin films using various nanoparticles.

TABLE OF CONTENTS

LIST OF FIGURES

LIST OF SCHEMES

NON-CONJUGATE POTENTIAL STEPPING PHENOTHIAZINE AND PHENOXAZINE BASED POLYMER HOLE-TRANSPORT MATERIAL FOR DYE-SENSITIZED SOLAR CELLS

Introduction:

The current world and local news indicate that global warming brought on through the use of fossil fuels that feed the ever increasing demand for energy, has expanded the global view concerning the environment and the energy needed for an industrialized society. The world energy demand is currently projected to increase by 70% from 2000 to 2030. At this growth rate, the fossil fuel supply will be depleted within 200 years based on current projections.[1, 4] Although, the debate on when the fossil fuel supply will be exhausted is still ongoing, the environmental impact of fossil fuels appears to be a major, global problem. These concerns have placed alternative energy research on top of the technical-development priority list resulting in exploration and development in everything from wind power, to harnessing the rise and fall of the tides. However, even with these alternative energy sources, generating enough power to satisfy the future global energy needs may be impossible. However, the sun is an enormous source of energy that radiates energy onto the earth at a rate $3x10^{24}$ J per year, which is far greater than the current world demand of $5x10^{20}$ J per year.[2] Currently, power production using existing solar technology is too expensive to be used by the general population, thus limiting its applicability.

Background:

In 1991, Michael Grätzel published a paper that introduced a new, functional version of the TiO_2 based dye-sensitized solar cells (DSSCs), which were previously unsuitable for real world applications. This paper described the problems of previous DSSCs, with extremely low energy conversion efficiencies and cell component instability. Since this paper was published there have been many reports describing DSSC and component variations using cells that are similar to the Grätzel cell.[1,3-6]

There are five main components that make up a DSSC. Starting at the top of the cell is a transparent electrode, which is required to allow penetration of solar radiation into the cell. The next component is the TiO_2 film, which is the semiconductor used to pick up electrons. Coating the TiO_2 film is the sensitizer (dye), generally a ruthenium tris(bipyridine) complex. The cell also contains a solution of electrolytes and finally the counter electrode. The DSSC functions in the following way: First, the sensitizer absorbs photons that entering into the cell through the transparent electrode. The absorption of the photons excites an electron from the sensitizer into the conduction band of the, TiO_2. After the removal of the electron from the sensitizer to the TiO_2, the electrolyte (mediator, generally I^-/I_3^-) will donate an electron to fill the hole created in the sensitizer. The electron in TiO_2 will then be transferred to the transparent electrode, while the hole (in the form of I_3^-) is transferred to the counter electrode, where it is reduced thus completing the circuit and generating electricity (See Figure 1, taken from reference 4).

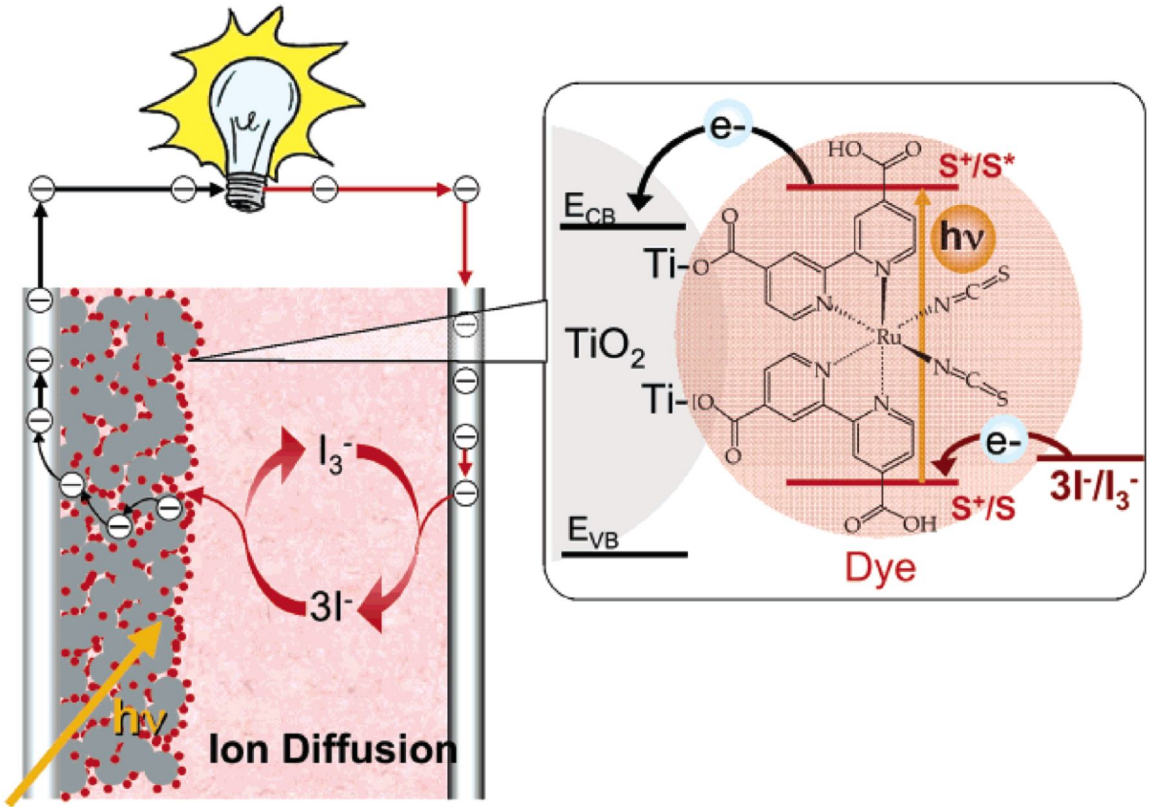

Figure 1.1: Schematic drawing showing the overall function of a dye sensitized solar cell. The dye is cis-$Ru(SCN)_2L_2$ (L = 2,2′-bipyridyl-4,4′-dicarboxylate).(Reprinted from reference 4)

Over time, each of the five main components has been replaced by various derivatives and alternatives in attempts to increase the stability, decrease price, and increase cell performance. For example, the sensitizer or dye has had a variety of bis(bipyridine) ligand derivatives placed around the ruthenium center to improve charge separation;[5] the ruthenium center has also been replaced with other metals such as zinc and copper to decrease the cost.[7] Metal-free, organic sensitizers have also been used. Some of these changes to the dye have resulted in the increase of efficiency and/or the decrease in cost of the solar cells. [5,8,11] The TiO_2 semiconductor film has also been replaced with other metal oxides such as ZnO or SnO_2 which have all been incorporated into the cells as a variety of different nanostructures, such as nanotubes, nanofibers or spherical particles with a vast range in size, in an attempt to increase efficiency and reduce cost .[5,9]

The other major component of DSSCs is the mediator, which is the primary cause for physical instability in the cells. The most commonly used electrolyte is I^-/I_3^- dissolved in a organic solvent, such as acetonitrile. If the cell cracks, the solvent will leak into the environment, causing the cell to die, as well as creating an environmental problem. To overcome this problem, several different approaches have been taken to reduce or eliminate the need for volatile electrolyte solutions. Several groups have attempted to replace the electrolyte with room temperature molten salts and organic hole transporting materials, such as, 2,2,7,7-tetrakis(*N*,*N*-di-*p*-methoxyphenyl-amine) 9,9-spirobifluorene (OMeTAD).[10,12,13] However, a more common replacement for the electrolyte in DSSCs is a conductive polymer. Currently two primary methods exist for replacing the liquid electrolyte with polymers. The first method involves creating a gel with a polymer encapsulating the electrolyte, which has been successful with a variety of carbon-based and silicon-based polymers, giving conversion efficiencies as high as 6.58%.[10-13] The second method involves synthesizing a conducting polymer with little to no solvent in the polymer matrix to create a stable platform. Several groups have synthesized a variety of solid conductive polymers using this technique even some silicon-based, with the highest efficiency reported at only 3.1% for high power conversion efficiency. The purpose of this part of the thesis, is to create a new conducting polymer based on the second method.[10,14-16]

The primary focus of this project is to replace the electrolyte with a hole-conducting, solid state, polymer, that will enable a similar electron tunneling process that occurs in DNA.[16,17] To explain this further, the base pairs in the central helix of the DNA strand reside in a tightly ordered π-stacked arrangement that serves as an efficient charge transportation route for electron tunneling through the system.[16,17] The electron conductivity of the DNA occurs in similar manner to graphite electron conductivity, in these π-stacked systems two aromatic rings stacked

on top of one another juxtaposes the p orbitals from the π bonds close enough to allow electrons to jump from one aromatic ring to another, thus, enabling conductivity (see Figure 2).

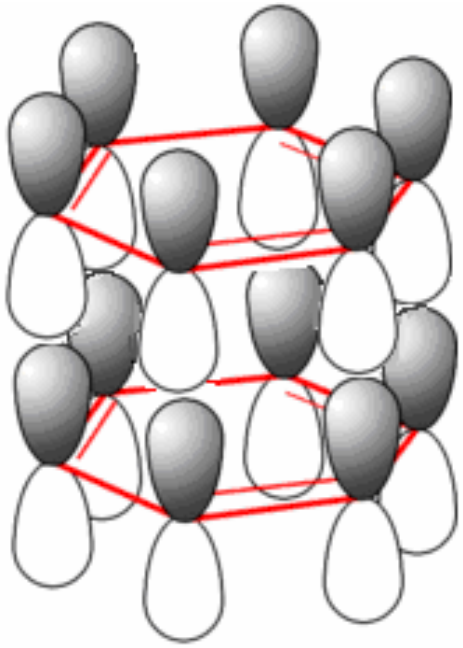

Figure 1.2*:* Two benzene molecules with p orbitals indicating the π bonds stacking which allows the orbitals to overlap allowing for conductivity.

The goal of this research is to mimic DNA and graphitic systems by incorporating, phenothiazine (PTZ) and phenoxazine (POZ) moieties into a polymer and enable a similar π-stacked arrangement with the added functionality of a redox-potential step in this block co-polymer. To understand a redox-potential stepping block co-polymer, a block co-polymer must be defined, as well as how application of the redox-potential step will affect its function in a DSSC. A block co-polymer is composed of two or more monomers. Each type of monomer is polymerized separately to create the block, and then the blocks composed of the different monomers are linked together to create the block co-polymer. In this case, the block co-polymer is composed of a PTZ and a POZ block to create the polymer with a single junction. The PTZ and the POZ groups will be attached to the polymer back bone, which allows these groups to π-stack and enable electron tunneling as shown in Figure 3.

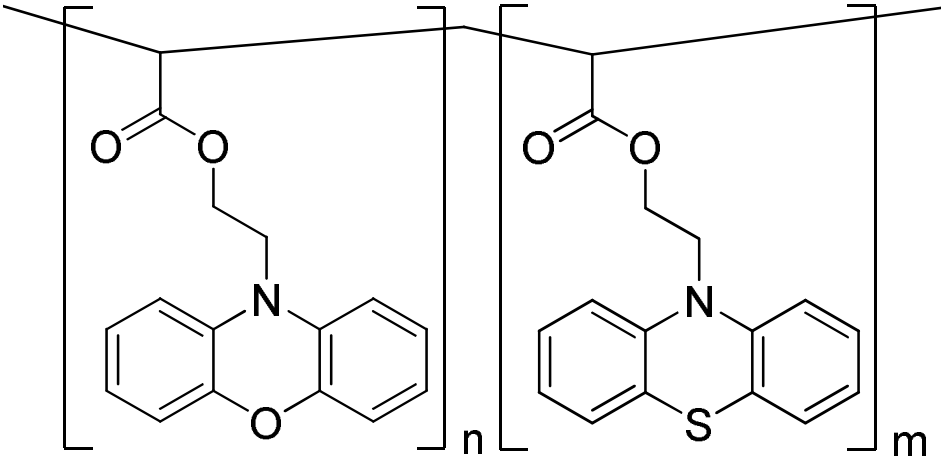

Figure 1.3: Representation of the polymer sections where the phenothiazine block meets the phenoxazine block.

The concept behind the redox-potential step has to do with the different oxidation potentials of POZ and PTZ. By synthesizing a co-polymer composed of two blocks one of the POZ monomers and the other of the PTZ monomers, a redox-potential gradient will occur at the junction of the two blocks. The reduction potentials of POZ and PTZ are 0.632 and 0.717 V vs. SHE (standard hydrogen electrode), respectively. Therefore, a hole injected into the PTZ block should become trapped on the POZ, thus creating a charge separated system. In DSSCs, if the POZ block is attached to the counter electrode, while the PTZ block is attached to or in close proximity to the dye, the hole generated on the dye should be able to tunnel through the polymer chain to the counter electrode.

Experimental Methods:

All reagents and solvents were used as received from Sigma-Aldrich and Fisher Scientific unless stated otherwise. All tetrahydrofuran (THF) was distilled prior to use. ^{1}H-NMRs were performed on a Varian Gemini 2000 broadband 300 MHz NMR. All thin layered chromatography (TLC) was performed on glass backed silica gel plates. All experiments were

performed at −78.9 °C in an acetone/dry ice bath while under N_2 atmosphere, and allowed to return to room temperature over 12 hours unless otherwise stated.

Synthesis of 2-(10H-phenothiazin-10-yl)ethanol (PTZEtOH): The reaction flask was charged with ~3 mL diisopropylamine along with ~6 mL of dry THF, then ~8 mL of 1.6 M N-butyllithium in hexane was added over a period of 3 minutes to produce lithium diisopropylamine (LDA). A separate flask was charged with phenothiazine (1.52 g, 0.0076 mol) in 4 mL of dry THF, this was injected into the reaction flask. After 20 minutes ethylene oxide was added in excess to the reaction flask. The reaction was left to stir for 24 hours. To quench the LDA and ethylene oxide excess methanol was added. TLC was performed in 1:1 hexane and ethyl acetate; Unknown side products R_f = 0.0, PTZEtOH R_f = 0.54, PTZ R_f = 0.82. Purification through silica gel column chromatography was performed in 1:1 mixture of hexane and ethyl acetate. Yield 22%. ^{1}H-NMR 300MHz $CDCl_3$; 2.364(m,1); 3.895(t,2); 4.099(t,2); 6.899-6.986(m,4); 7.156-7.206(m,4).

Alternative Synthesis of 2-(10H-phenothiazin-10-yl)ethanol (PTZEtOH): This synthesis was adapted from the literature.[22] A mixture of phenothiazine (0.8248 g, 0.00414 mol) and ethylene carbonate (0.6793 g, 0.00774 mol) was heated to 200 °C for 12 hours. TLC was performed in 1:1 hexane and ethyl acetate; PTZEtOH R_f = 0.54, PTZ R_f = 0.82.

Synthesis of 2-(10H-phenothiazin-10-yl)ethyl acrylate: The reaction flask was charged with 2-(10H-phenothiazin-10-yl)ethanol (0.477 g, 0.0196 mol) and 4.5 mL of toluene, then 0.3 mL of acryloyl chloride was added and left stirring for 24 hours. The solution was then

quenched with methanol and the solvent was removed in vacuo. Purification through silica gel column chromatography was performed in 1:1 mixture of hexane and ethyl acetate. Yield 15%. ^{1}H-NMR $CDCl_3$; 4.198(t,2); 4.519(t,2); 5.838, 5.878(dd,1); 6.094, 6.129, 6.152, 6.186(qd,1); 6.395, 6.457(dd,1); 6.921-6.972(m,4); 7.142-7.204(m.4).

Synthesis of 2-(10H-phenoxazin-10-yl)ethanol: The reaction flask was charged with ~4 mL diisopropylamine, ~10 mL of dry THF, then ~10 mL of 1.6 M N-butyllithium in hexane was added over a period of 3 minutes to produce lithium diisopropylamine (LDA). A separate flask was charged with phenoxazine (0.4 g, 0.0020 mol) in 4.5 mL of dry THF, this was injected into the reaction flask. After 20 minutes ethylene oxide was added in excess. The reaction was left to stir for 24 hours. To quench the LDA and ethylene oxide excess methanol was added. Purification through silica gel column chromatography was performed in 1:1 hexane ethyl acetate. ^{1}H-NMR $CDCl_3$; 3.501(s,l); 3.734(t,2); 3.925(t,2); 6.602-6.673(m); 6.768-6.814(m).

Results and Discussion:

The first step in the synthesis of 2-(10H-phenothiazin-10-yl)ethanol (PTZEtOH) resulted in a 22% yield suggesting that alternative methods may be needed to increase the yields (see Scheme 1). The yield for the 2-(10H-phenoxazin-10-yl)ethanol (POZEtOH) was unobtainable due to sample loss, from destruction of the vial containing the product, only enough was recovered to run the NMR. ^{1}H NMR spectra were checked for these two precursors in deuterated chloroform $CDCl_3$ giving triplets at 4.00 ppm and 3.88 ppm for PTZEtOH and 3.93 ppm and 3.76 ppm for POZEtOH, which indicates the attachment of the ethane chain to the nitrogen on the PTZ and the POZ as seen in Figure 4.

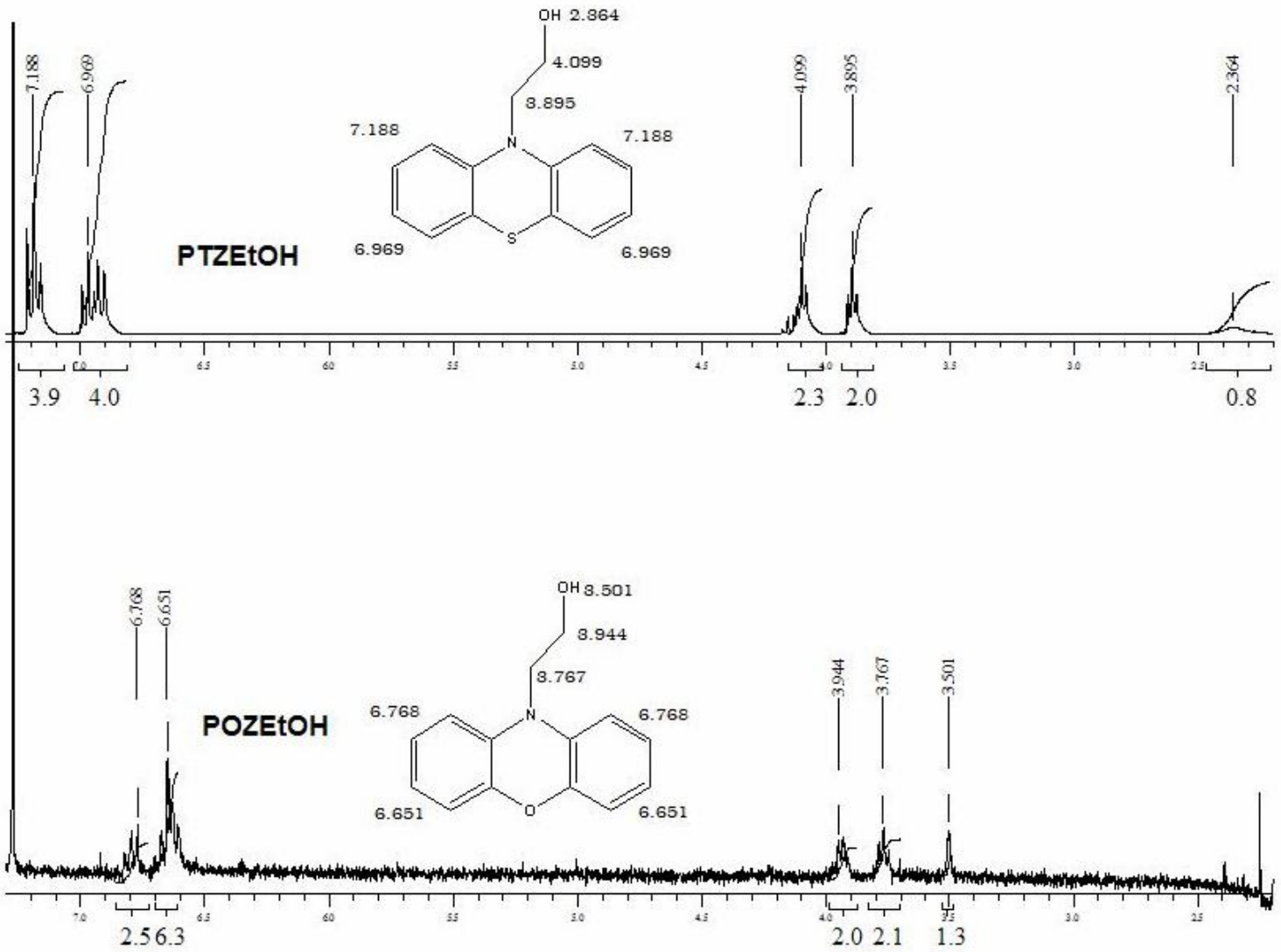

Figure 1.4: ^{1}H NMR spectra of the functionalized PTZ and POZ monomers precursors (referenced to the solvent peak). Top: 2-(10H-phenothiazin-10-yl)ethanol in $CDCl_3$, 2.408(m,1); 3.888(t,2); 4.091(t,2); 6.899-6.986(m,4); 7.156-7.206(m,4). Bottom of ^{1}H NMR 2-(10H-Phenoxiazin-10-yl)ethanol in $CDCl_3$, 3.501(s,l); 3.734(t,2); 3.925(t,2); 6.602-6.673(m); 6.768-6.814(m) (large amount of noise seen here is due to the low concentration of the product in the solvent).

The alternative synthesis for PTZEtOH was performed to eliminate side products and to eliminate the use of ethylene oxide, due to its volatility.[22] The thin layer chromatography indicated presence of PTZEtOH and the elimination of side products with no R_f at zero. However, most of the PTZ remained in the reaction as starting material, resulting in the inability to obtain a yield.

The conversion of the PTZEtOH to produce 2-(10*H*-phenothiazine-10-yl)ethyl acrylate (the PTZ monomer) occurred with a 15% yield. The low yield could be due to the hydrochloric acid produced when the reaction takes place causing the degradation of the PTZEtOH. The addition of an organic base, such as pyridine, should neutralize the acid and increase the yield as outlined in Scheme 1.

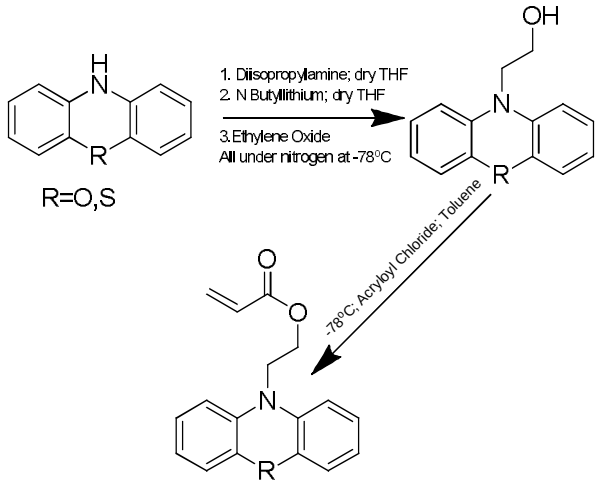

Scheme 1.1: The overall reaction scheme for the synthesis of the acrylate monomers.

The ^{1}H NMR of the PTZ monomer showed seven groups of peaks indicating the structural characteristic of the monomer. Starting up field the peaks at 4.198 (t,2) and 4.519 (t,2) are from the ethane chain. The acryl peaks are 5.838, 5.878 (dd,1) for the beta hydrogen that is cis to the double bonded oxygen, 6.094, 6.129, 6.152, 6.186 (qd,1) for the alpha hydrogen and 6.395, 6.457 (dd,1) for the beta hydrogen away from the double bonded oxygen. The peaks for the phenothiazine group are 6.921-6.972 (m,4) and 7.142-7.204 (m.4) as shown in Figure 5.

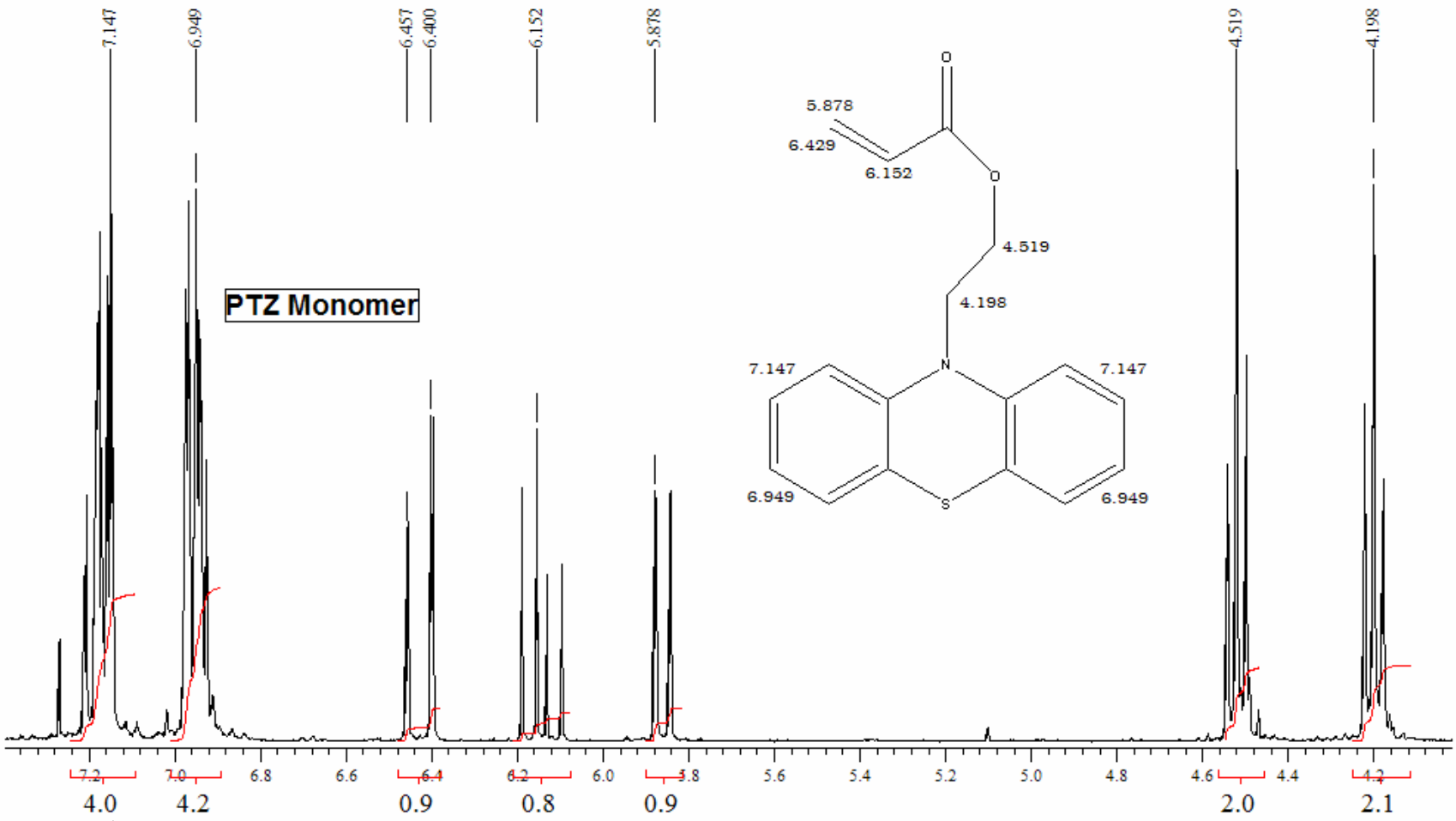

Figure 1.5: ^{1}H NMR spectra of the functionalized PTZ monomer. NMR of 2-(10H-Phenothiazin-10-yl)ethyl acrylate in $CDCl_3$: 4.198(t,2); 4.519(t,2); 5.838, 5.878(dd,1); 6.094, 6.129, 6.152, 6.186(qd,1); 6.395, 6.457(dd,1); 6.921-6.972(m,4); 7.142-7.204(m.4).

An observation was made with regards to the synthesis of each of the PTZ containing compounds, that a pink byproduct is produced in each synthesis. It was determined that the pink byproduct was the oxidation of the PTZ indicating another possible route for product loss leading to low yields and other possible side reactions.

Conclusion:

In conclusion, the PTZEtOH, POZEtOH and PTZ ethyl acrylate monomer were successfully synthesized and characterized. It was observed that the oxidation of the synthesized products as well as the precursors poses a problem with decreasing yield as well as a possible acid degradation problem with the monomer synthesis. These issues can be addressed with tighter controls on the atmosphere and the introduction of a base such as pyridine. The successful characterization of these products through NMR and TLC show the peak splitting and position as well as TLC elution position that will be of use in future work when looking for future and alternative syntheses.

Future work on this project will consist of finding and alternative syntheses to PTZEtOH and POZEtOH due to current problems with the volatility of ethylene oxide and the low yields. Alternative monomers for the eventual synthesis of the potential stepping block co-polymer will be explored to increase the rigidity of the polymer backbone. One such possibility would be to follow the synthesis of a similar PTZ based polymer. Schrock and coworkers synthesized a PTZ polymer with bis(2-(10H-phenothiazin-10-yl)ethyl) bicyclo[2.2.1]hept-5-ene-2,3-dicarboxylate as the monomer. By replacing 2-(10H-phenothiazin-10-yl)ethanol with 2-(10H-phenoxazin-10-yl)ethanol in the synthesis one could potentially produce bis(2-(10H-phenoxazin-10-yl)ethyl) bicyclo[2.2.1]hept-5-ene-2,3-dicarboxylate and have both of the monomers to produce block co-

polymer with Schrocks' living ring opening metathesis synthesis.[18] Once a polymer has been made, the structural and hole transpiration properties can be tested using spectroscopic methods, such as, nuclear magnetic resonance (NMR) and electron paramagnetic resonance (EPR). NMR can be used to determine the structural orientation of the PTZ and POZ with respect to the π-stacking interactions. EPR can be used to track electron movements and to determine if the hole was completely delocalized through the polymer.[23] Eventually the polymer must be attached to an electrode, which will lead to the possible integration of this polymer into various electronics such as DSSCs.

REFERENCES:

1) Li, B.; Wang, L.; Kang, B.; Wang, P.; Qiu, Y. *Sol. Energ. Mat. Sol. C.* **2006**, *90*, 549-573.
2) Grätzel, M. *Nature* **2001**, *414*, 338-346.
3) O'Regan, B. Grätzel, M.; *Nature* **1991**, *353*, 737-740.
4) Grätzel, M. *Inorg. Chem*. **2005**, *44*, 6841-6851.
5) Yum, J. H.; Chen, P.; Grätzel, M.; Nazeeruddin, M. K. *ChemSusChem* **2008,** *1*, 699-707.
6) Grätzel, M.; *C. R. Chimie* **2006**, *9*, 578-583.
7) Robertson, N. *ChemSusChem* **2008**, *1*, 977-979.
8) Mishra, A.; Fischer, M. K. R.; Bäuerle, P. *Angew. Chem. Int. Ed.* **2009**, *48*, 2474-2499.
9) Ghicov, A.; Schmuki, P. *Chem. Commun*. **2009**, 2791-2808.
10) Nogueira, A. F.; Longo, C.; De Paoli, M.-A. *Coordin. Chem. Rev.* **2004**, *248*, 1455-1468.
11) Sharma, G. D.; Balraju, P.; Kumar, M.; Roy, M. S. *Mater. Sci. Eng. B* **2009**, *162*, 32-39.
12) Bach, U.; Lupo, D.; Comte, P.; Moser, J. E.; Weissörtel, F.; Salbeck, J.; Spreitzer, H.; Grätzel, M. *Nature* **1998**, *395*, 583-585.
13) Snaith, H. J.; Schmidt-Mende, L. *Adv. Mater.* **2007**, *19*, 3187-3200.
14) Xiang, W.; Zhou, S.; Yin, X.; Xiao, X.; Lin, Y.; Fang, S. *Polym. Adv. Technol.* **2009**, *20*, 519-523.
15) Shin, W. S.; Kim, C. S.; Lee, S. J.; Jeon, H. S.; Kim, M. K.; Naidu, B. V. K.; Jin, S. H.; Lee, J. K.; Lee, J. W.; Gal, Y. S. *J. Polym. Sci. Part A: Pol. Chem.* **2008**, 1394-1402.
16) Merino, E. J.; Boal, A. K.; Barton, J. K. *Curr. Opin. Chem. Biol.* **2008**, *12*, 229-237.
17) Harriman, A. *Angew. Chem. Int. Ed.*, **1999**, 38, 945-949.
18) Albagli, D.; Bazan, G.; Wrighton, M. S.; Schrock,R. R. *J. Am. Chem. Soc.* **1992**, 114, 4150-4158.
19) Labaye, D. E.; Jėrôme, C.; Geskin, V. M.; Louette, P.; Lazzaroni, R.; Martinot, L.; Jėrôme, R. *Langmuir* **2002**, *18*, 5222-5230.
20) Malinauskas, A. *Polymer* **2001**, *42*, 3957-3972.
21) Nguyen, V.; Yoshida, W.; Jou, J. D.; Cohen, Y. *J. Polym. Sci. Pol. Chem.* **2001**, *40*, 26-42.
22) Kamogawa, H. *J. Polym. Sc:. Part A-1*, **1972,** *10*, 95-101.
23) Rathore, R.; Abdelwahed, S. H.; Kiesewetter, M. K.; Reiter, R. C.; Stevenson, C. D. *J. Phys. Chem. B* **2006**, *110*, 1536-1540.

INCREASING VOID SPACE IN POROUS TiO_2 TO STUDY DIFFUSION PROPERTIES WITH COBALT MEDIATORS

Introduction:

As modern technology becomes cheaper and more abundant, things like personal computers, cell phones, and various other electronic gadgets are available to the masses on scales never before seen. Therefore, the demand for energy to power all these technological advancements has increased to a staggering $5x10^{20}$ J per year.[1] The vast majority of the current energy demands have thus far been met by the use of fossil fuels such as coal, oil and natural gas.[2] However, pollution associated with fossil fuels is a big draw back of their use. For example in 2009, US coal fired power plants released about 48 tons of mercury and 1,876.8 million metric tons of CO_2 into the atmosphere.[3,4] The release of heavy metals, such as mercury, into the environment as well as various sulfates, nitrates, and carbon dioxide have resulted in the development of environmental problems we have yet to fully understand. Since fossil fuels are causing major environmental problems, an alternative energy source that does not pollute the environment as a byproduct of its energy production is needed to reduce the environmental impacts.

One alternative energy source exists that has the potential to reduce or eliminate emissions as well as supply the modern world with enough energy to send it into the 22^{nd} century and perhaps beyond. This source of energy is the sun, which has been supplying $3x10^{24}$ J of energy per year to this planet for billions of years.[1] To harness this power source, single crystal silicon solar cells have been used with current efficiencies of ~25.0 %. However, these solar

cells are hard to produce and expensive.[5] An alternative to silicon based solar cells is the dye sensitized solar cells (DSSCs), which are made out of much cheaper materials than their silicon counterparts.

Background:

The basic construction of a dye sensitized solar cell (DSSC) consist of five primary parts: the conductive glass anode, a TiO_2 thin film on the glass anode, the dye, mediator, and the cathode.[1] In recent studies, cobalt mediators have been substituted for the iodide/triiodide (I^-/I_3^-) mediator that has been most commonly used for DSSCs in the past do to its high efficiencies and good overall cell performance. The corrosive and volatile nature of the (I^-/I_3^-) mediator is the primary reason for researching a viable replacement. The cobalt mediators are not volatile nor corrosive, and their structural and redox properties can be tuned to optimize electron transfer via structural modifications of the ligands, which make them a suitable alternative to the I^-/I_3^-.[6] However, DSSCs incorporating cobalt mediators have shown to be diffusion limited which has effected cell performance with lower steady state currents, fill factors, and conversion efficiency.

The diffusion limitations are evident when studying the current transient response of the cell; in current transient experiments light is pulsed on and the current is measured with respect to time at short circuit. In a DSSC with iodine mediator, the current transient is square shape which indicates that the cell reaches its steady state immediately upon illumination. In a cell where the mediator is diffusion limited, the current spikes initially then steadily decays down to the steady state current.

It was shown by Nelson and coworkers that DSSCs were limited by the diffusion of the Co(III) complex diffusing out of the TiO_2 thin film to the cathode.[7] This was shown by the

broadening of the current spike and the increase in the steady state current when the concentration of Co(III) complex was increased from 0.008 M to 0.03 M concentration as shown in Figure 1.[7] This suggests that the diffusion of the Co(III) complex from the dye out of the TiO_2 to the cathode was the main limiting factor in the diffusion.

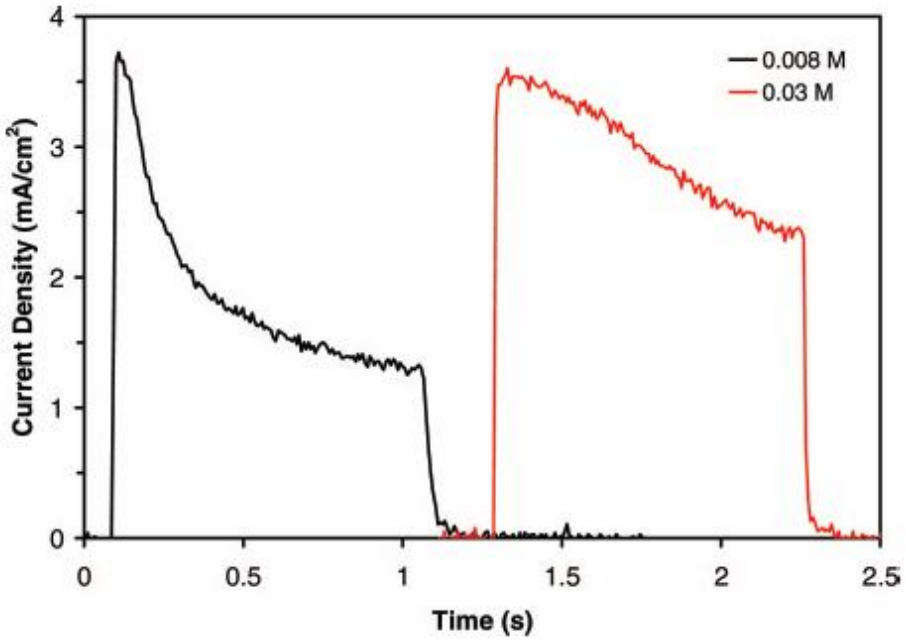

Figure 2.1: Current transients of cobalt mediated DSSCs with varying concentrations. Graph in black was the cobalt mediator with a concentration of 0.008 M. Graph in red was the cobalt mediator with a concentration of at 0.03 M. Reproduced from reference 7.

The article written by Feldt and coworkers proposes that as the size of the cobalt complex increases, the mass transport of the mediator is retarded in the system.[8] This suggests that by increasing pore size or by rearranging the TiO_2 film into structures like nanowires may facilitate diffusion into and out of the TiO_2 thus eliminating or reducing the mass transport issues of the cobalt mediated DSSC.

In this paper, void space is introduced into TiO_2 films by incorporating nanoparticles into the TiO_2 slurry, then subsequently removing the nanoparticles from the film after the slurry is doctor bladed onto fluorine-doped tin oxide (FTO) glass (transparent electrode). The cobalt

mediator used for all photovoltaic tests in this report is $[Co(DTB)_3](ClO_4)_3$ (where DTB = 4,4′-di-tert-butyl-2,2′-bipyridine) along with *cis*-di(thiocyanato)-bis(4,4′-dicarboxy-2,2′-bipyridine)ruthenium(II) dye, also known as N3 dye, shown in Figure 2.

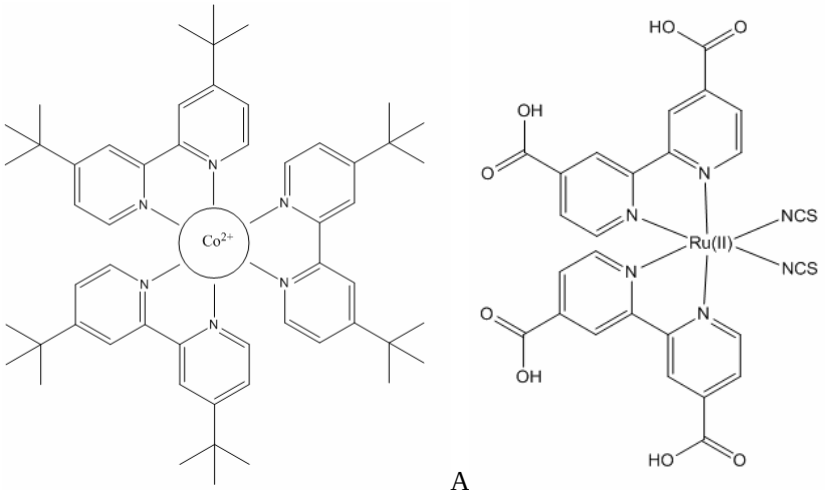

A B

Figure 2.2: Structures of cobalt mediator and ruthenium dye. Diagram A is of $Co(DTB)_3^{2+}$ (where DTB = 4,4′-di-tert-butyl-2,2′-bipyridine). Diagram B is of *cis*-di(thiocyanato)-bis(4,4′-dicarboxy-2,2′-bipyridine)ruthenium(II) dye.

Four types of nanoparticles were introduced into different TiO_2 slurries which were doctor bladed onto FTO glass to create TiO_2 films and then removed from the films to introduce void space. The four types of nanoparticles used were polystyrene nanoparticles (100 nm), magnetite (Fe_3O_4) at (9 nm and ~100 nm sizes), iron nanowires, and nickel nanowires. The ferromagnetic nanoparticles were aligned with an applied magnetic field in an effort to create oriented channels that permeate the entire film, which, from current literature searches, has not been performed before.

Experimental Methods:

All reagents and solvents used were received from Sigma-Aldrich or Fisher Scientific unless stated otherwise.

All scanning electron microscopy (SEM) images were taken with JEOL JSM-6500F Field Emission Scanning Electron Microscope. All digital images of films were captured with an Olympus Stylus 800 8.0 megapixel digital camera. Photovoltaic data was monitored with a Keithley 2400 Source Meter controlled by Labview Virtual instrument connected via a two electrode configuration. The light source for the photovoltaic data was a 100-150 W Oriel arc lamp made by Oriel Instruments Model 66002 with an Oriel Cornerstone 1/8 m Monochromator Model 74000. The light was passed through a 400 nm cutoff filter to prevent direct excitation of TiO_2. Current-Voltage (CV) measurements were taken with white light. Labview virtual instrument controlled wavelength selection was employed when incident photon to current efficiency (IPCE) measurements were taken. The potentiostats used for the electrodeposition and electrochemical measurements were a BAS-100 and a HCH Instrument Electrochemical Analyzer model CHI1232A, respectively. Vapor deposition of metals was performed with a Denton Vacuum BTT-IV and a T Maxtek, Inc. MDC-260 Deposition Controller. All profilometry data was obtained from a Bruker Dektak XT profilometer with a 12.5 μm stylus unless other wise stated.

All FTO glass was cleaned by sonicating in a saturated solution of Alconox biodegradable surfactant for $\leq$ 30 min. The FTO was then rinsed with distilled water to remove all the surfactant, acetone, and dried with N_2 or Gust Easy Duster (pure 1,1-difluoroethane).

Doctor blading of the TiO_2 slurry was performed on clean FTO glass that was cut into 7x5 cm rectangles using the "one scotch" method as follows. These rectangles were scored into ten 1.2x2.5 cm segments on the nonconductive side with the two segments on one end of 1x2.5 cm. Tape was applied along either edge of the FTO glass, conductive side up. Slurry was

applied to the 1x2.5 cm segments and a glass rod was used to spread the slurry. The slurry was allowed to dry in air prior to being annealed at 450 °C for 1 hour unless otherwise stated.

All photovoltaic cells were dyed with N3 dye as follows. Prior to use in a cell, the photoanodes were reheated to 180 °C (note that the nickel containing films were reheated to 450 °C for only a few minutes before being allowed to cool to 130 °C). At this point, the still-hot anodes were immersed in a saturated ethanol (200 proof) solution of N3 dye and left over night. The anode was removed from the dye solution, rinsed with ethanol and dried under a stream of nitrogen immediately before use.

Cobalt mediator solutions were prepared by dissolving 35.9 mg of $[Co(DTB)_3](ClO_4)_2$, 4.4 mg of $[Co(DTB)_3](ClO_4)_3$ and 7.9 mg lithium trifluoromethanesulfonate (triflate) in 250 µl of γ-butyrolactone containing 7 µl of tert-butylpyridine. New cobalt solutions were prepared every two weeks to ensure accurate ratios of mediator.

All DSSC experiments were conducted using a sandwich cell configuration. A cathode (thermally evaporated gold-on-chromium-on-FTO glass) was placed on top of the dyed anode. One drop of mediator solution was applied outside the gap between the anode and cathode and subsequently drawn into the interior of the cell by capillary action. The assembly was then placed into a custom made cell holder and fixed with a screw clamp. An FTO extension (with conducting copper tape) was clamped to the anode to facilitate electrical connection. The aperture on the cell holder has a 0.385 cm^2 area.

Incorporation of Polystyrene nanoparticle:

The method for polystyrene nanoparticle incorporation was a modification of the method reported by Birnie and co-workers.[9-11] The polystyrene nanoparticles were provided by Duke

Scientific Corporation and capped with carboxyl ligands. The slurry was assembled from Solaronics T37 Slurry (0.3448 g), a solution of polyethylene glycol 800 (PEG, 0.1324 g, 0.1 wt%), triton X-100 (0.0764 g, 0.1% v/v), and 100 nm polystyrene carboxyl (0.0527 g, 4% v/v). The slurry was vortexed, then sonicated for 30 min. The sample was centrifuged at 11000 rpm for 4 min. and the supernatant was removed. The sample was vortexed and sonicated again to re-suspend the slurry (earlier attempts that omitted this step resulted in incomplete films that had exposed FTO glass). The slurry was then doctor bladed onto clean FTO glass using the method described above. SEM and digital camera images, as well as photovoltaic data were taken. Profilometry data was obtained with the use of a Sloan Dektak IID profilometer (catalog: 139960, serial: 03018 4/84) and a Sloan Dektak IID controller (catalog: 139960, serial: 03021 5/84).[9-11]

Synthesis of Magnetite nanoparticles:

Synthesis of ~9 nm particles: This synthesis followed the procedure of Jin and co-workers.[12] The nanoparticles were characterized using TEM. In order to transfer the nanoparticles from the hexanes into water, ethanol (0.5 mL, 95 %) was added to a 1 mL aliquot of the hexane solution and centrifuged at 4000 rpms for 1 min to crash out the nanoparticles. The supernatant was removed and the remaining solvent was removed in vacuo for >12 hrs at room temperature. The nanoparticles were placed in 1 mL of a citric acid solution (1.0433 g citric acid/10 mL H_2O).[13]

Synthesis of ~100nm particles: This synthesis was a modification of the procedure reported by Nishio and coworkers.[14] The synthesis starts by degassing a solution of ferrous chloride (0.1 *M* $FeCl_2$, 50 mL) and a solution of $NaNO_3$/NaOH (1.5746 g $NaNO_3$, 21 m*M* NaOH,

1 L), then cooling the solutions to ~6 °C. Once cooled, 50 mL of the $NaNO_3$/NaOH solution was removed and discarded before adding the $FeCl_2$ solution. The mixture was stoppered and vigorously shaken, before leaving the solution overnight at ~6 °C. A magnet was placed on the outside of the container to pull the magnetite nanoparticles out of solution. The nanoparticles were washed with degassed H_2O (1 L, x3). After washing, a Triton X-100 solution in water (3 mL, 0.1 % v/v) was mixed with the nanoparticles and dried in a vacuo for >12 hrs at room temperature.[14]

Preliminary P25 slurry with magnetite nanoparticles from the 100 nm syntheses:

To an aliquot of the P25 slurry (0.5 mL, 18 wt%) was added 10 drops of the ~100 nm magnetite mixture. The sample was vortexed then doctor bladed onto clean FTO glass and quickly placed into a ~2 tesla magnetic field, where it remained until dried (ca. 45min.). Samples were annealed at either 450 °C, 300 °C, or left at room temperature. After annealing, samples were placed into a 0.5 *M* solution of oxalic acid for one hour. SEM and digital images were taken before and after annealing and acid wash of the samples.

Synthesis of Iron Nanowires:

The synthesis of iron nanowires was adapted from literature procedures by Lin and coworkers and by Hachred and coworkers.[15,16] A 1.0 L solution was prepared consisting of $FeSO_4 \cdot H_2O$ (0.863 *M*), H_3BO_3 (0.73 *M*), and ascorbic acid (0.0057 *M*) at pH of 3.0. Any solids that did not dissolve were removed by decanting the solution. The BAS 100 was used to grow the wires set with the STEP method using the following parameters Initial E:-700 mV, High E: -700 mV, Low E:-1000 mV, Initial Scan Direction: Negative, Pulse width: 200 msec, Sensitivity:

100 µA/V, Number of cycles: 900, Quiet Time: 2 sec. The deposition was performed in a water-cooled, jacketed, electrochemical cell to maintain the solution at room temperature. The working electrode was a 0.2 µm Whatman Anodisc 13 first coated with 5 nm of chromium then with 100 nm gold, vapor deposited on back of the template. The Whatman Anodisc 13 was attached to a coiled copper wire with silver paste on the vapor deposited gold side. All non-plating surfaces were coated with a nitrocellulose/acetone paste for insulation. The counter electrode was iron mesh and the reference electrode was a sodium chloride saturated calomel electrode (SSCE). After deposition, the coatings were dissolved in acetone and the template was repeatedly washed with acetone. The 0.2 µm Whatman Anodisc was dissolved in a 0.5 M NaOH solution. SEM images, as well as, EDS data was taken of the resulting nanowires.[15,16]

Synthesis of Nickel Nanowires:

A solution consisting of $NiSO_4$ (46.01 g/100 mL), $NiCl_2$ (7.37 g/100 mL), and H_3BO_3 (4.028 g/100 mL) with a pH~0 was used.[17,18] The HCH Instruments Electrochemical Analyzer potentiostat or a AA battery was used for the synthesis of these nanowires. When performing the synthesis with the HCH Instruments Electrochemical Analyzer the potentiostat was set to: Amperometric i-t Curve, Parameters: Init E (V): -1.5, Sample Interval (sec): 1, Sampling time (sec): 10-70 min, Quiet time (sec): 0, Sensitivity (A/V): 1e-002. The working electrode was 0.2 µm Whatman Anodisc with 100-200 nm silver deposited on one side. Electrical contact to the silver was made with copper tape. All non-plating surfaces where coated with a nitrocellulose/acetone paste for insulation. The counter electrode was nickel wire and the reference electrode was a sodium chloride saturated calomel electrode (SSCE). After deposition, the coatings were dissolved in acetone and the template was repeatedly washed in acetone. The

silver was removed with HNO_3 and Whatman Anodisc was dissolved in a 0.5 M NaOH solution. The freed nanowires were suspended in ethylene glycol. SEM images were taken of the resulting nanowires.[17,18]

Synthesis of P25 Degussa Slurry and Films:

The slurry synthesis was adopted from Smestad and coworkers and Asobatzis and coworkers.[19,20] The synthesis was modified to decrease the amount of slurry produced and avoid cracking of the film. A mixture of P25 Degussa (~0.5 g) and acetylacetone (e.c. acac, 0.1-0.2 mL) in 0.6-0.9 mL distilled H_2O was ground with a mortar and pestle until no lumps were visible. To the mixture, distilled H_2O (0-1.7 mL) was added slowly and ground to maintain a smooth paste; followed by the addition of 1-3 drops or 20-300 µL of Triton X-100 and additional grinding to create a uniform distribution. For some samples the Triton X-100 was added before the second addition of water. The slurries were doctor bladed onto clean FTO glass. SEM images were taken and profilometry data was obtained after annealing.[19,20]

Incorporation of Nickel Nanowires into P25 Slurry (Referred to as "nickel films"):

The nickel nanowires were washed with distilled H_2O and then with acetone to remove the ethylene glycol, and dried in vacuo for >12 hrs at room temperature. The nanowires were weighed, Triton X-100 (~10 µL) was added, and the sample was sonicated until wires were re-suspended (≥48 hrs). The P25 slurry was made using the same methods as described above and 0.5-1.5 mL was added to the nanowire suspension. The sample was sonicated for ≤ 48 hours, vortexed then doctor bladed onto clean FTO glass, then quickly placed into a ~2 tesla magnetic field while still wet. The samples were allowed to dry in the field for 45 minutes. Dried samples

were annealed at 450 °C. After annealing, samples were placed into a 1:5 solution of concentrated nitric acid and concentrated hydrochloric acid for ≤ 72 hours to remove the wires. SEM and digital images were taken of the samples before and after annealing and acid wash. EDS and profilometry data was collected as well.

Results and Discussion:

Using Polystyrene Nanoparticles to Introduce Void Space:

The SEM images in Figure 3 show the 100 nm void space resulting from the incorporation and subsequent removal (by oxidation during the 450°C annealing steps in air) of the 100 nm polystyrene nanoparticles. The relative distribution appears essentially uniform as viewed in the SEM images below. In the first SEM image, the relative distribution can be observed by the dark spots throughout the surface indicating the void space left behind from the polystyrene nanoparticles.

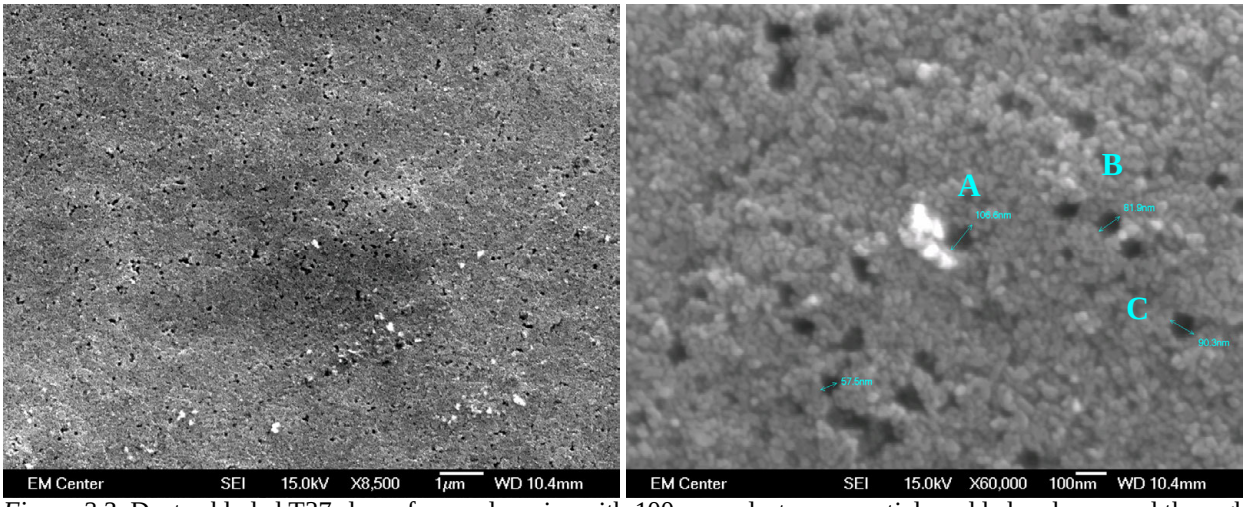

Figure 2.3: Doctor bladed T37 slurry from solaronics with 100 nm polystyrene particles added and removed through annealing at 450°C. Image to the left is zoomed out to x8,500, image to the right zoomed into x60,000 with measured pores, A at 106.6 nm, B at 81.9 nm and C at 90.3 nm.

These films did not adsorb a lot of the N3 dye and the dye did not adsorb uniformly, which could indicate that the TiO_2 films are not uniform with respect to the macro scale. The digital images in Figure 4 show the non-uniformly distributed dye on the test samples.

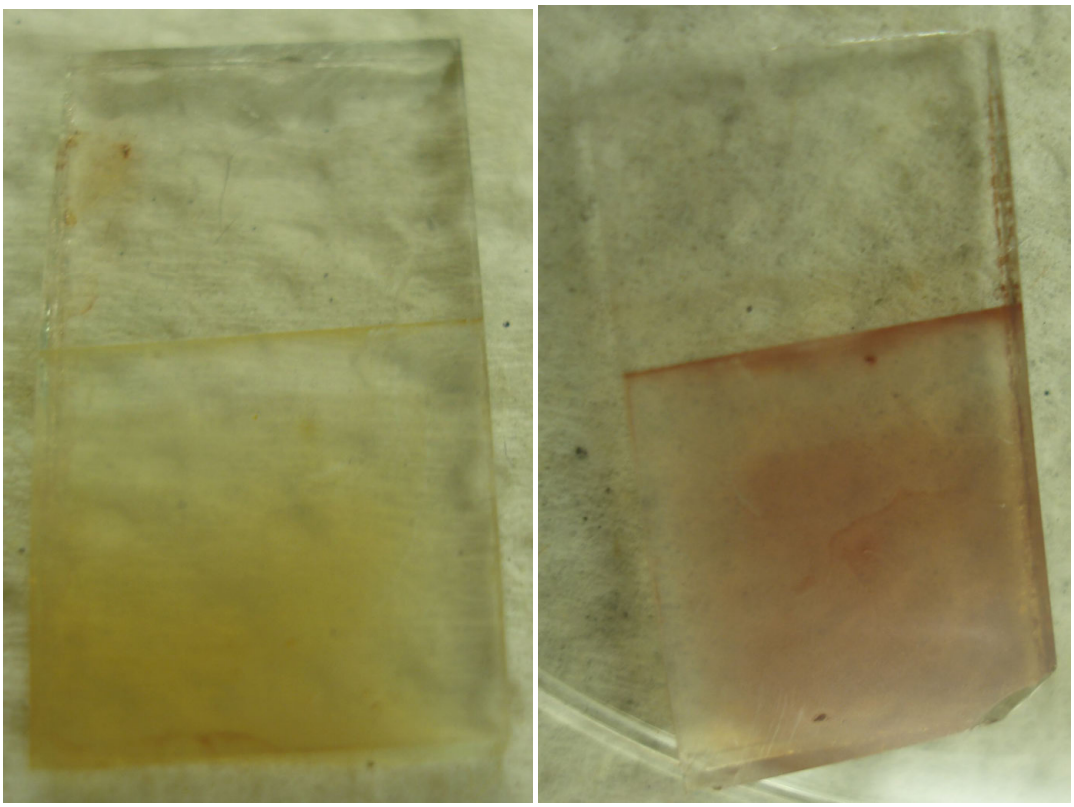

Figure 2.4: Digital images of N3 dyed TiO_2 T37 films with void space introduced by 100 nm polystyrene nanoparticles. Picture on the left shows the first sample a week after being dyed. Picture on the right shows the second sample shown two days after being dyed.

The profilometry data indicated that these were extremely thin films (~200 nm). However, the stylus on the profilometer dug into part of the film rendering the calculated film thickness suspect.

Similarly, films have been made using the polystyrene nanoparticles in the past.[9,10,11] Since this method of introducing void space into the TiO_2 films produces poor quality films and specifically the polystyrene nanoparticles are unable to be aligned to create channels further efforts along this line were abandoned. The focus of this research was switched to using

ferromagnetic nanoparticle systems that can be aligned using a magnetic field to create channels of void space in the TiO_2 films.

Using Ferromagnetic Nanoparticles to Introduce Void Space: ~9 nm Magnetite (Fe_3O_4) Nanocrystals

The magnetite nanoparticles were imaged using TEM, which confirmed the ~9 nm sized magnetite nanocrystals as shown in Figure 5. However, 9 nm is right on the edge of the TEM sensitivity so an accurate measure of the particle size and a reliable standard deviation is not possible to obtain. A digital photo was taken of the solution containing the nanoparticles suspended in hexane with a magnet placed along the side of the container which is also shown in Figure 5. The image demonstrates that the whole solution moves in the magnetic field rather than causing the nanoparticles to precipitate out of solution. This type of response suggests that the solution is a ferrofluid. However, attempting to place the ~9 nm magnetite particles into an aqueous solution causes the nanoparticles to oxidize into hematite (Fe_2O_3) indicated by the rust red color. Unfortunately, hematite is non-magnetic. Due to this oxidation issue the larger (~100 nm) magnetite nanoparticles with a smaller surface area to volume ratio, were synthesized in an aqueous solution.

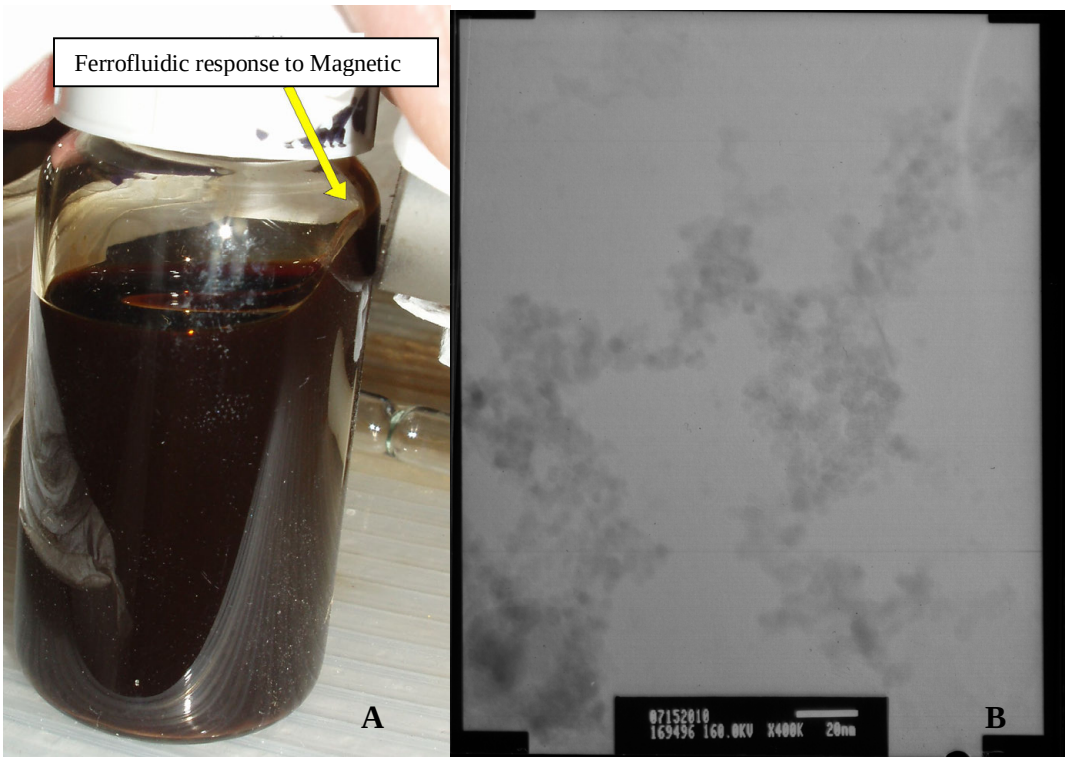

Figure 2.5: Images of the ~9 nm magnetite particles. Image A is of the ~9 nm magnetite particles in a hexane with a magnet on the side of the vial demonstrating its ferrofluidic properties. Image B is the TEM image of the nanoparticles confirming the ~9 nm particle size.

Using Ferromagnetic Nanoparticles to Introduce Void Space: ~100 nm Magnetite Nanoparticles:

The synthesis of the ~100 nm particles in an aqueous solution simplifies their introduction into the TiO_2 thin films since the slurries are already in an aqueous medium. The various test films were either annealed at 450°C, 300°C, or left at room temperature. Figure 6 shows digital images of the samples annealed at the three temperatures. The change from magnetite to hematite in the 450°C and 300°C film samples is indicated from the color change from black to red. After treating with oxalic acid, the films have a red tint indicating the presence of iron. The films were also rubbed with a finger, which showed that the 450°C films are the most abrasion resistant. It is also noteworthy that only one sample of the room temperature treated films survived the acid treatment; all others resulted in the film flaking off the FTO glass.

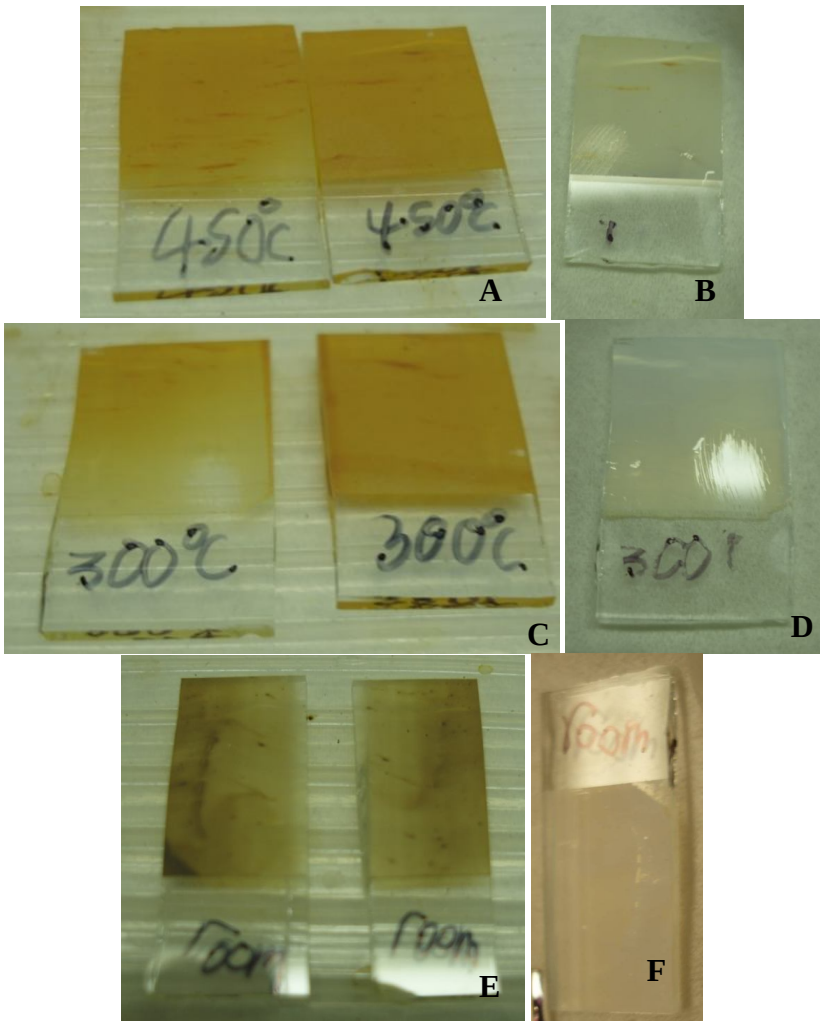

Figure 2.6: Images of magnetite films. Images A and B are of samples annealed at 450 °C. Image B shows the sample after being treated with oxalic acid and the results of the abrasion test, which appears as a scrape on the lower left of film. Images C and D are of samples annealed at 300 °C. Image D shows the sample after being treated with oxalic acid and the results of the abrasion test, which appears as a scrape on the lower right of film. Images E and F are of samples left at room temperature. Image F shows the film after being treated with oxalic acid. No abrasion test was done on this sample because it was the only sample to survive the oxalic acid treatment for room temperature acid treated samples.

The SEM and EDS images in Figure 7 show that the size of the assumed 100 nm magnetite nanoparticles was actually closer to 1 μm than 100 nm (image A) that the literature suggested, and the EDS image map (image B) of the same region indicates where the largest deposits of iron are located. The void space created by the removal of a magnetite nanoparticle with oxalic acid is shown in image C. A quick visual scan of the surface with SEM showed that the magnetite particles vary in size from ~100 nm to ~4.0 microns.

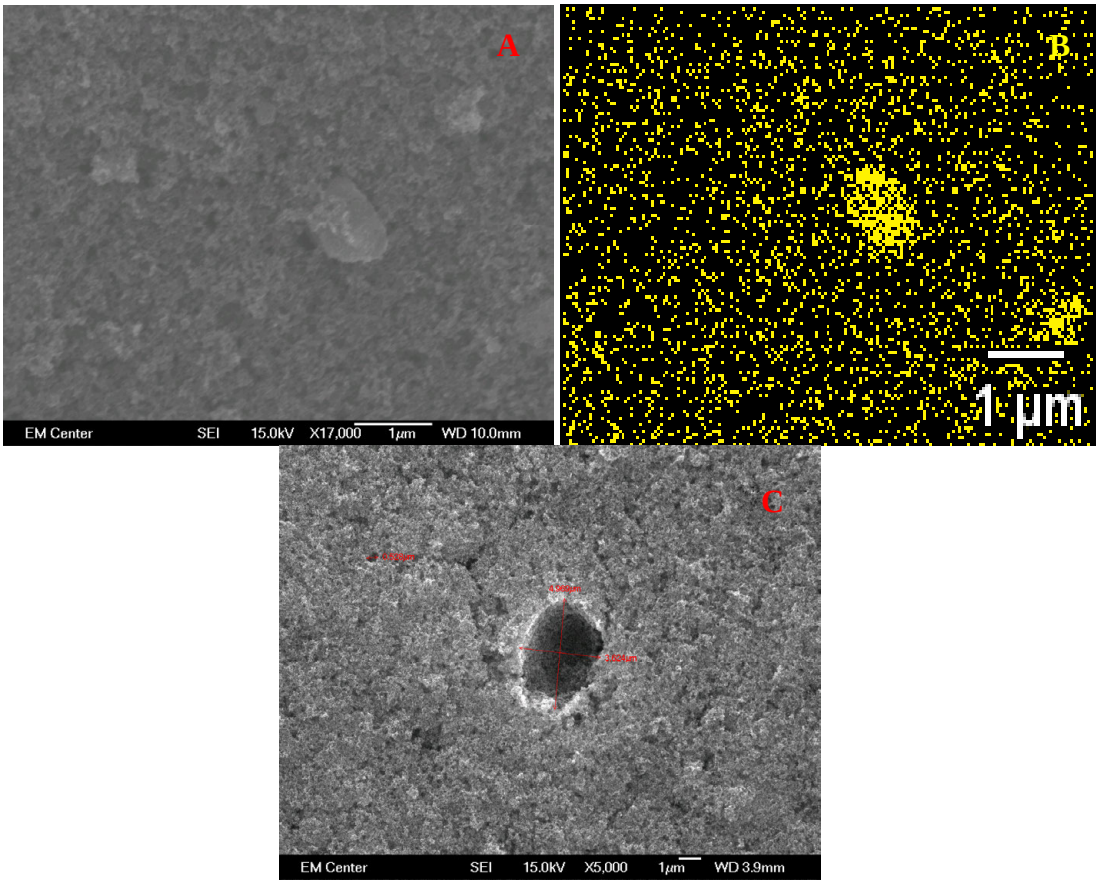

Figure 2.7: SEM images of P25 films with the assumed 100 nm magnetite nanoparticles and the void space introduced by their removal. (A) P25 films before treatment with oxalic acid showing intact nanoparticles of magnetite with an approximate size of 1 micron. (B) The EDS image map of the iron in the SEM image of A. (C) P25 films after annealing and oxalic acid treatment showing the dimensions of the void space left after the removal of the nanoparticle. Note actual magnetite nanoparticles appeared as a range of 100-4000 nm sizes.

Since this method of void space integration produced red tinted films due to iron oxide contamination and lacked defined nanoparticle alignment, this method was also abandoned. In order to ensure the formation of the channels in the films, the focus of this research was switched to using nanowires to create highly aligned channels in the TiO_2 films instead of relying on the alignment of nanoparticles.

Using Nanowires to Incorporate Highly Aligned Channels of Void Space into TiO_2 Films: Iron Nanowires

The synthesis used to produce the iron nanowires was successful; however, the very large surface area of these wires makes them extremely susceptible to oxidation. The nanowires quickly oxidize in air even while being removed from the alumina temple. An SEM image shown in Figure 8 was obtained from the remainder of the nanowires that were not still attached to the gold backing. They were extremely short considering the template is approximately sixty microns thick and the nanowires should have extended close to the full length.

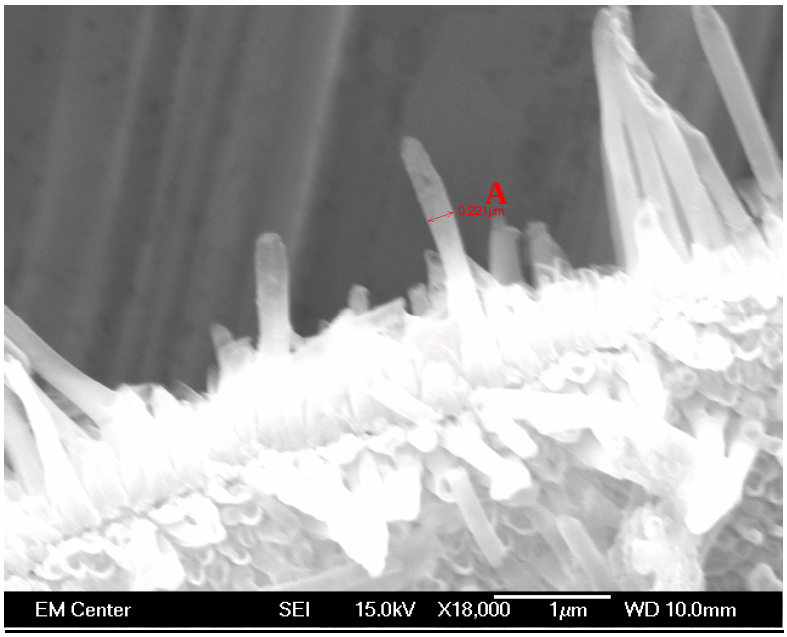

Figure 2.8: SEM image of the iron nanowires attached to a gold substrate, wires A is 221 nm. Point EDS was performed on the nanowires confirming the presents of iron in the wires.

Due to the extreme sensitivity to oxygen that the iron nanowires display, it was decided to move to nickel nanowires since nickel is much more resistant to oxidization than iron.

Using Nanowires to Incorporate Highly Aligned Channels of Void Space into TiO_2 Films:

Nickel Nanowires:

The synthesis used to produce the nickel nanowires resulted in uniform growth with a linear relationship in time: for example, it took ten minutes to grow ~10-14 µm nanowires and 30 minutes to grow ~32-35 µm as shown in Figure 9.

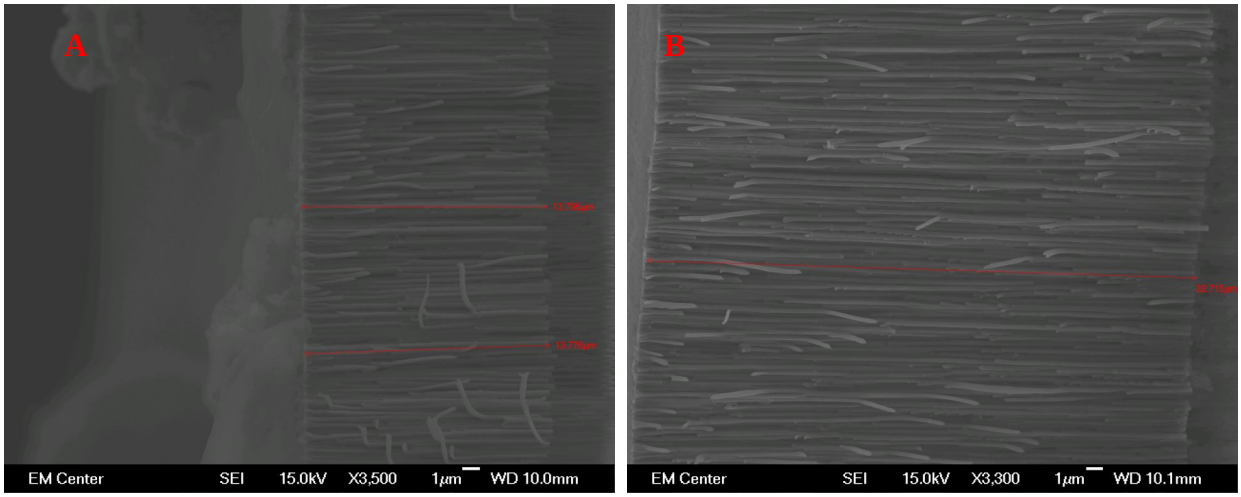

Figure 2.9: SEM images of nickel nanowire growth, side view or wires in Al_2O_3 template. Image A is an SEM image of a sample with a deposition time of 10 min. giving ~13 µm sized nanowires.. Image B is an SEM image of a sample with a deposition time of 30 min. resulting in ~32 µm sized nanowires. On the left side of the images is where the electrical contact as made, to the center the nickel nanowires have grown in the template, and to the right is the alumina template

However, some of the templates resulted in non-uniform growth and more unpredictable growth times. To solve this problem, the vapor deposited silver layer on the template was increased from 100 nm to 200 nm to ensure conductivity and the deposition solution was changed out when solution became cloudy. This resulted in controlled, uniform growth, which allowed the continuation onto TiO_2 slurry synthesis and growth.

Synthesis of P25 Degussa Slurry:

A variety of slurry preparations were attempted to try and produce thin films without cracks in the films. However, there appears to be no discernable pattern with the P25 slurry preparations regarding their ability to produce non-fractured films. A slurry preparation method will produce smooth films one day, and then on a different day the same preparation method, new slurry, produces cracked films. This issue with cracked films may be the result of the small scale of the preparations. On such small scales any minor difference can impart big changes to the overall product. Also it should be noted that none of the literature based P25 slurry syntheses were performed on a scale requiring less than 1.5 grams of P25.

However, one of the P25 slurries synthesized produced a smooth surface and was composed of 0.5992 grams of P25, 0.1 mL acac in 0.9 mL of H_2O, to which was added 0.5 mL H_2O along with 20 µl of Triton X-100. SEM images of this film showing the smooth uniform surface are given in Figure 10. Another film which cracked during the synthesis is also shown in Figure 10 as a comparison. The cracked film was formed from slurry composed of 0.5230 grams of P25, 0.1 mL acac in 1.0 mL of H_2O, to which was added 1.0 mL H_2O along with 1 drop of Triton X-100.

In these images the smooth film surface appears to be composed of nicely packed nanoparticles with an overall smooth surface (disregarding the TiO_2 clusters that sit on the surface left over from breaking the films during sample preparation). In comparison, the cracked films resemble dried mud, with large fissures all over the surface connected in an ever growing web.

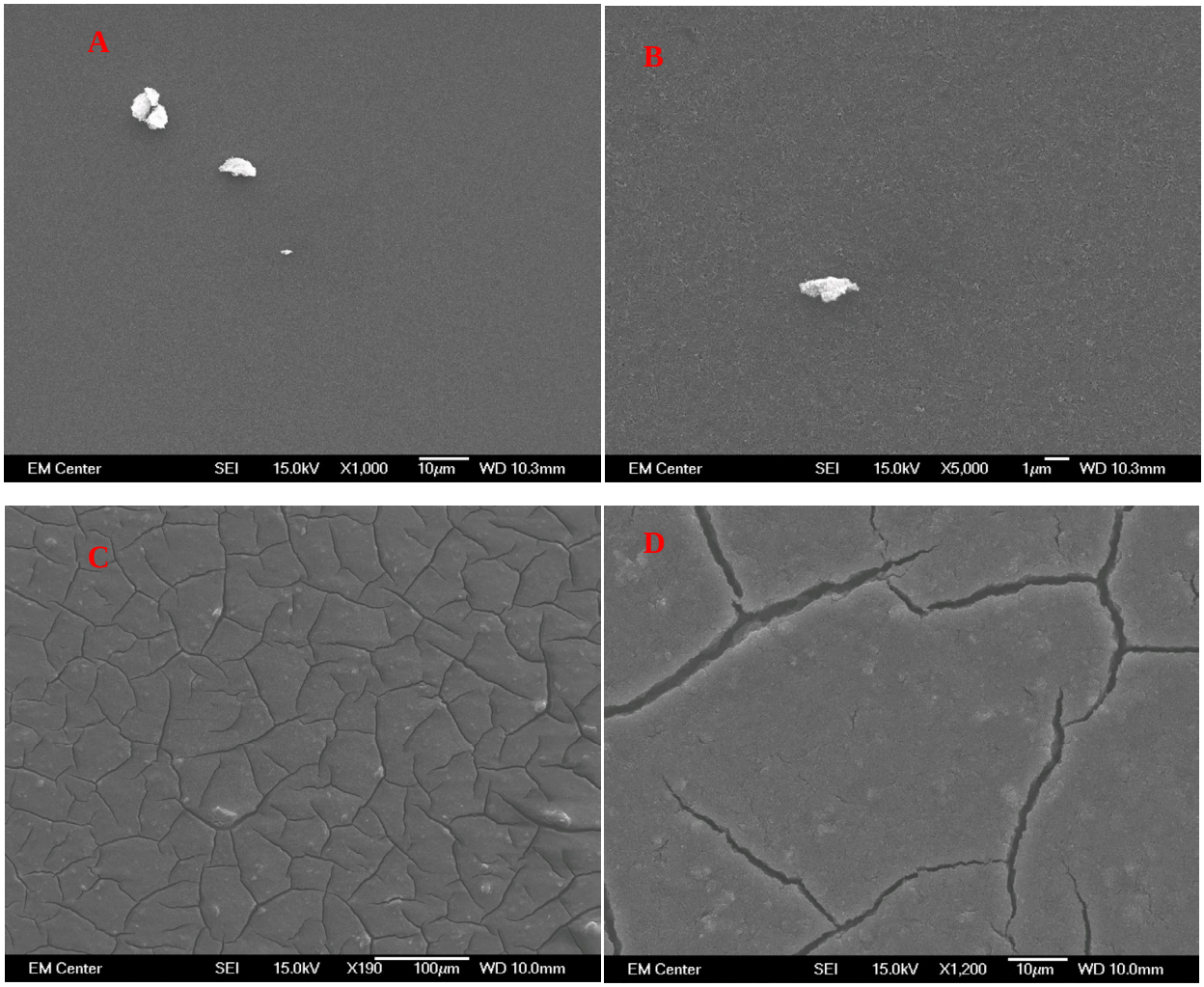

Figure 2.10: SEM images of P25 films without and with cracks. Images A and B are SEM images of the smooth slurry mentioned above. Images C and D are SEM images of the cracked surface of the slurry mention above.

Both the smooth film and the cracked film were dyed with N3 dye and used in DSSCs with cobalt mediator to compare their function. The digital images in Figure 11 of the smooth films show some uniformity for some of the samples, however, the color saturation varies between each film indicating variation in film thickness. The three cracked films, Figure 11 C, show similar uniformity when dyed.

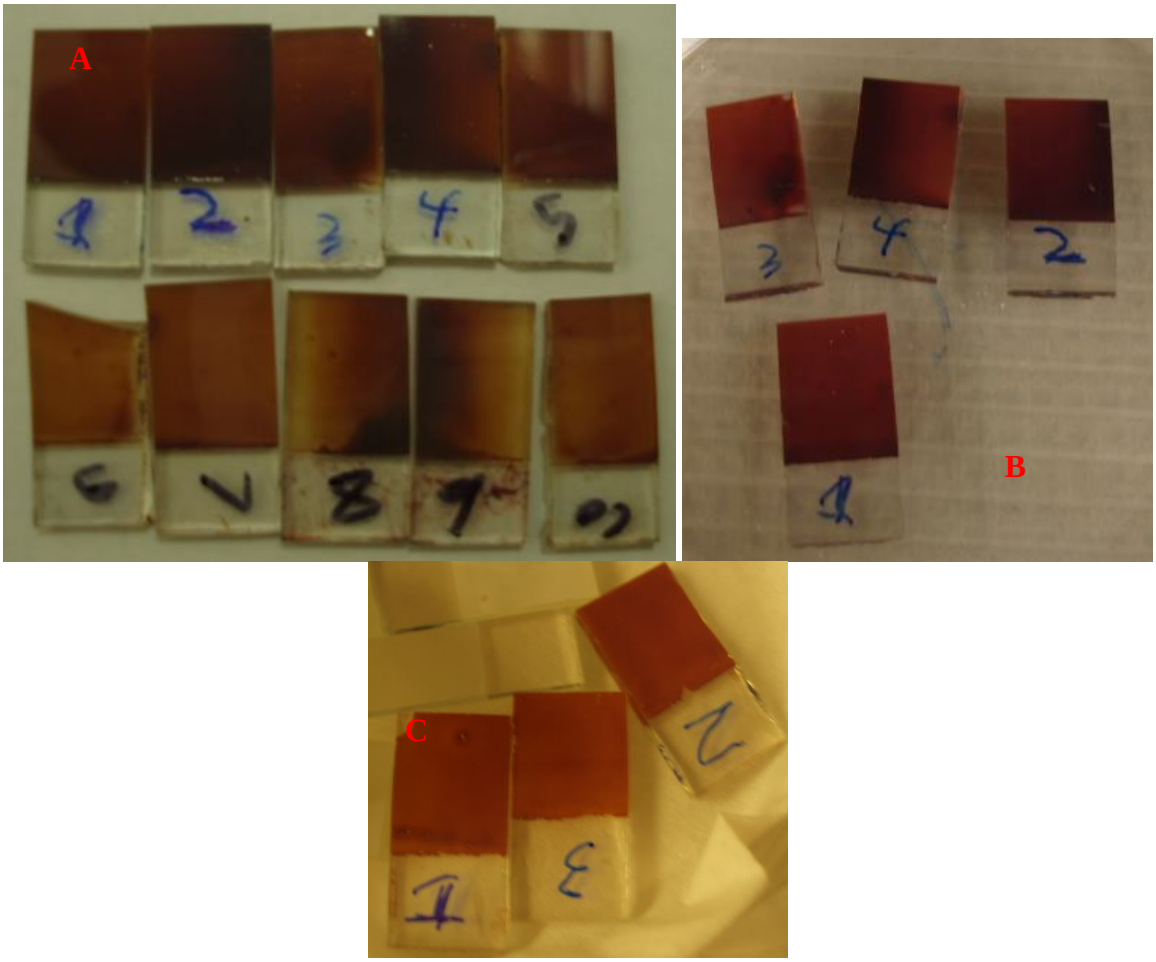

Figure 2.11: Digital images of the dyed smooth and cracked films. Images A and B are the dyed smooth films. Image C is the dyed cracked film.

Current transient data was used to determine the qualitative diffusion kinetics of the mediator in DSSCs. In current transient experiments light is pulsed on and the current is measured with respect to time at short circuit. The current transients obtained using the smooth and cracked films in cobalt mediated DSSCs are displayed in Figure 12 along with their thicknesses as determined by profilometry. In the DSSCs containing smooth films with thicknesses ≤ 5 µm, the current spike is greatly reduced. The small current spike indicates that the cell is not diffusion limited. This is likely due simply to the thinner film thickness rather than any improved mobility of mediator through the TiO_2 film. The goal of this project is to structure a film in away that improves the rate of cobalt mediator transport through the TiO_2 films, so it is

more relevant to compare the current transients of the thick, smooth films to the thick, cracked films (6-10.5 µm). There is a large difference in the current spike observed when comparing the current transients of the smooth versus the cracked films, which indicates that the rate of mediator diffusion increases with cracking as shown in Figure 12.

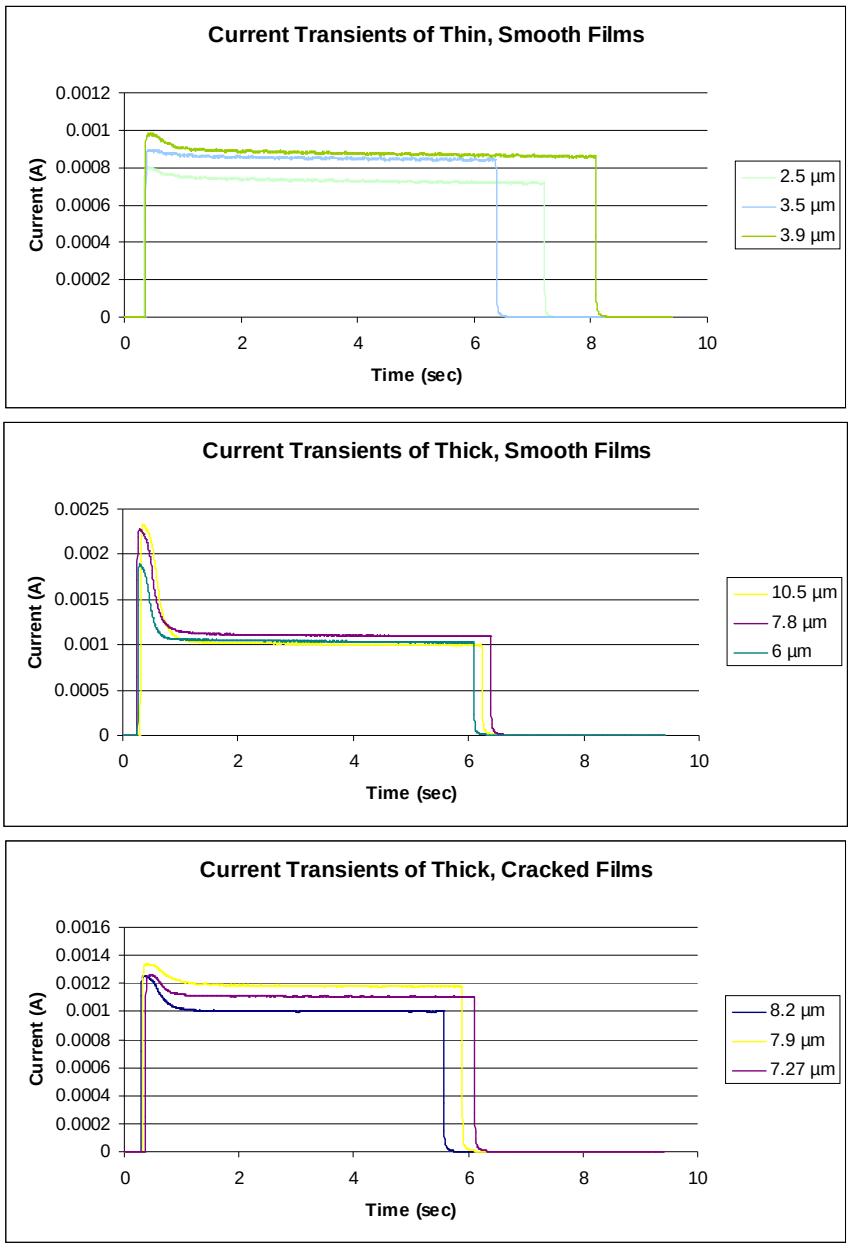

Figure 2.12: Current transients of the smooth and cracked films. The top graph is of all the thin smooth films. The second graph down is of the thick smooth films. The bottom graph is of the cracked films. All film thicknesses are displayed on the legend.

However, the steady state currents for each of the films are all about the same, this could be due to a light or dye-limited electron injection rate into the anode. The incident photon to current efficiencies (IPCEs) for the films, both the smooth and cracked, have the same overall slope with similar peaks and valleys occurring at the same wavelengths with the peak at 540 nm. However, when comparing the 7.8 µm smooth film to the 7.9 µm cracked film there is distinct differences in overall IPCE % magnitude of the two graphs, with the cracked film having a lower IPCE % overall. Looking at just the maximum peak of the graphs at 540 nm the smooth film was at 58.7 % IPCE and the cracked film is at 35.4 % IPCE about 40 % lower. This lower IPCE % maybe due to the missing TiO_2 resulting in missing dye in the cracked films which would also contribute to lowering the steady state current (see figure 13).

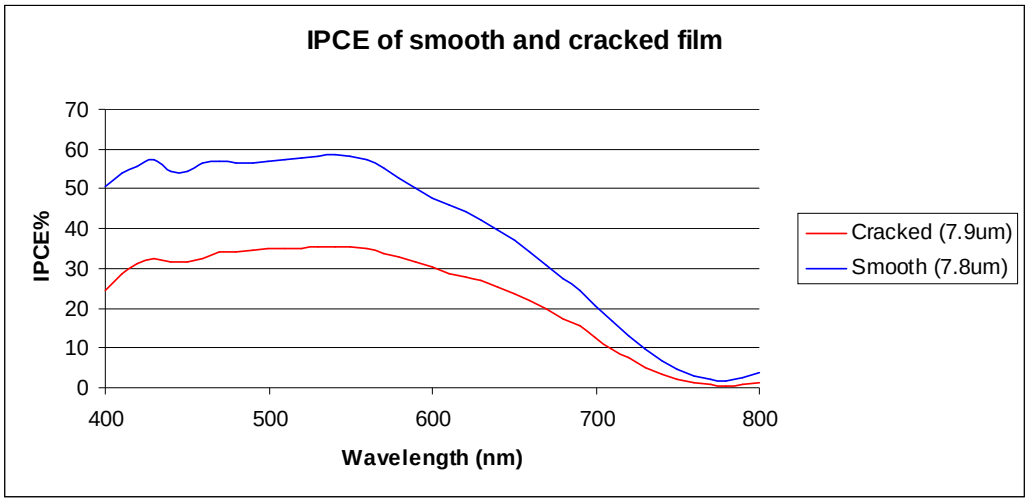

Figure 2.13: IPCE % Plot of smooth film in blue and cracked film in red. This comparison shows the cracked film with significantly lower IPCE % then the smooth film.

The voltage transients are similar for the smooth and cracked films as well with a steady state voltage at 0.5 V and decays to zero in 4-5 seconds. The current versus potential scans are also similar, showing short circuit currents (J_{sc}) in the range of 0.001-0.0012 A and open circuit voltages (V_{oc}) in the range of ~0.5 V as shown in Figure 14. The agreement between the IPCEs,

voltage transients and current vs. potential scans enables this data to be compared to the results of DSSCs containing films with void space created by nickel nanowires.

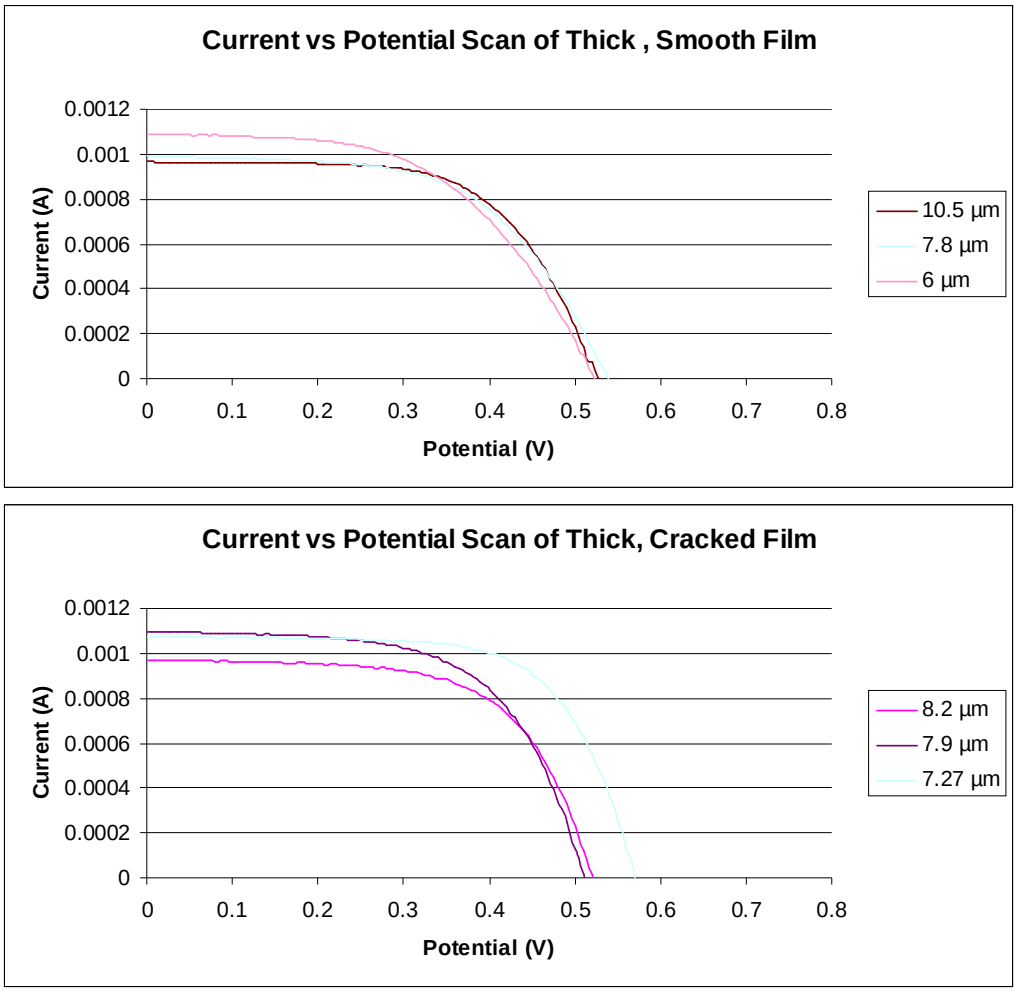

Figure 2.14: Current vs. potential scans of the thick smooth and cracked films. The top graph is of the smooth films. The bottom graph is of the cracked films.

DSSCs Using TiO_2 Films with Void Space Created by The Incorporation of Nickel Nanowires: Incorporation of Nickel Nanowires into P25 Slurry

The incorporation of nickel nanowires into the P25 slurry was attempted several times. SEM images were taken on the edge of one film to show the vertical alignment of the nickel nanowires in the TiO_2 film, which resulted from drying the films in an applied magnetic field of ~2 Tesla. The SEM images in Figure 15 A and B show at least two individual nanowires

standing essentially vertical, alone in the film, and image C shows two nanowires standing together with the longer wire being bent at the surface of the film. These images confirm that the magnetic field does indeed align the nanowires vertically in the films, at least to some degree. Without the magnetic field the nanowires lay on top of the surface of the film horizontally. Therefore, continued attempts were made to develop new films with more uniformly dispersed nickel nanowires, and without cracks or as large of cracks as in previous films.

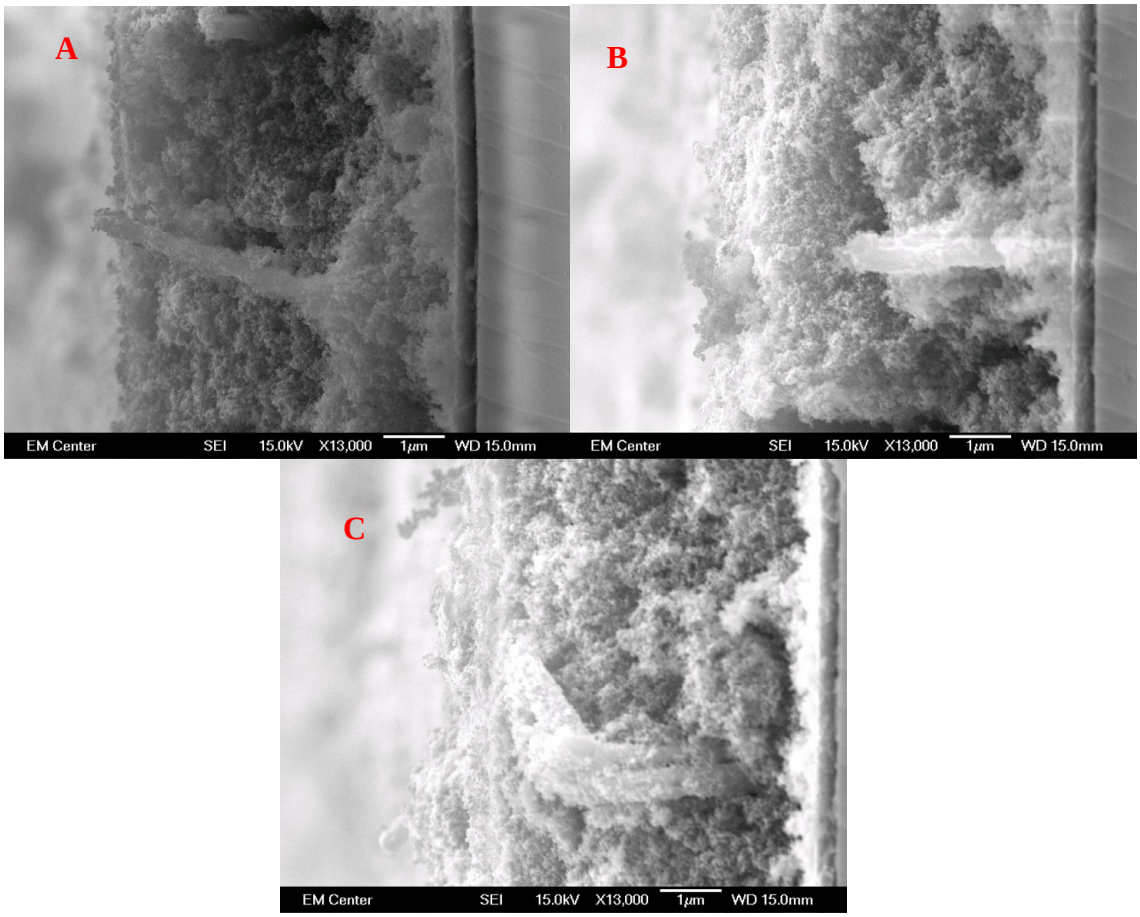

Figure 2.15: SEM images of the edge of the aligned nickel nanowires in the film.

The most recent attempt to disperse the nickel nanowires into the TiO_2 film employed a slurry composed of 0.0047 g nickel nanowires in 10 µl of Triton X-100 and had 0.5 mL of a P25 slurry composed of 0.5104 g P25, 0.1 mL acac in 0.9 mL H_2O, to which was added 100 µl of Triton X-100 and 0.5 mL H_2O, added to the wires. SEM images of the film surface shows the

dispersion of the nanowires through the film. However, there are some clusters that result in small cracks or just bundles in the film as shown in Figure 16. SEM images were also taken after removing the nanowires using the 5:1 HCl (concentrated) and HNO_3 (concentrated) acid solution, which indicates that the nanowires were removed successfully.

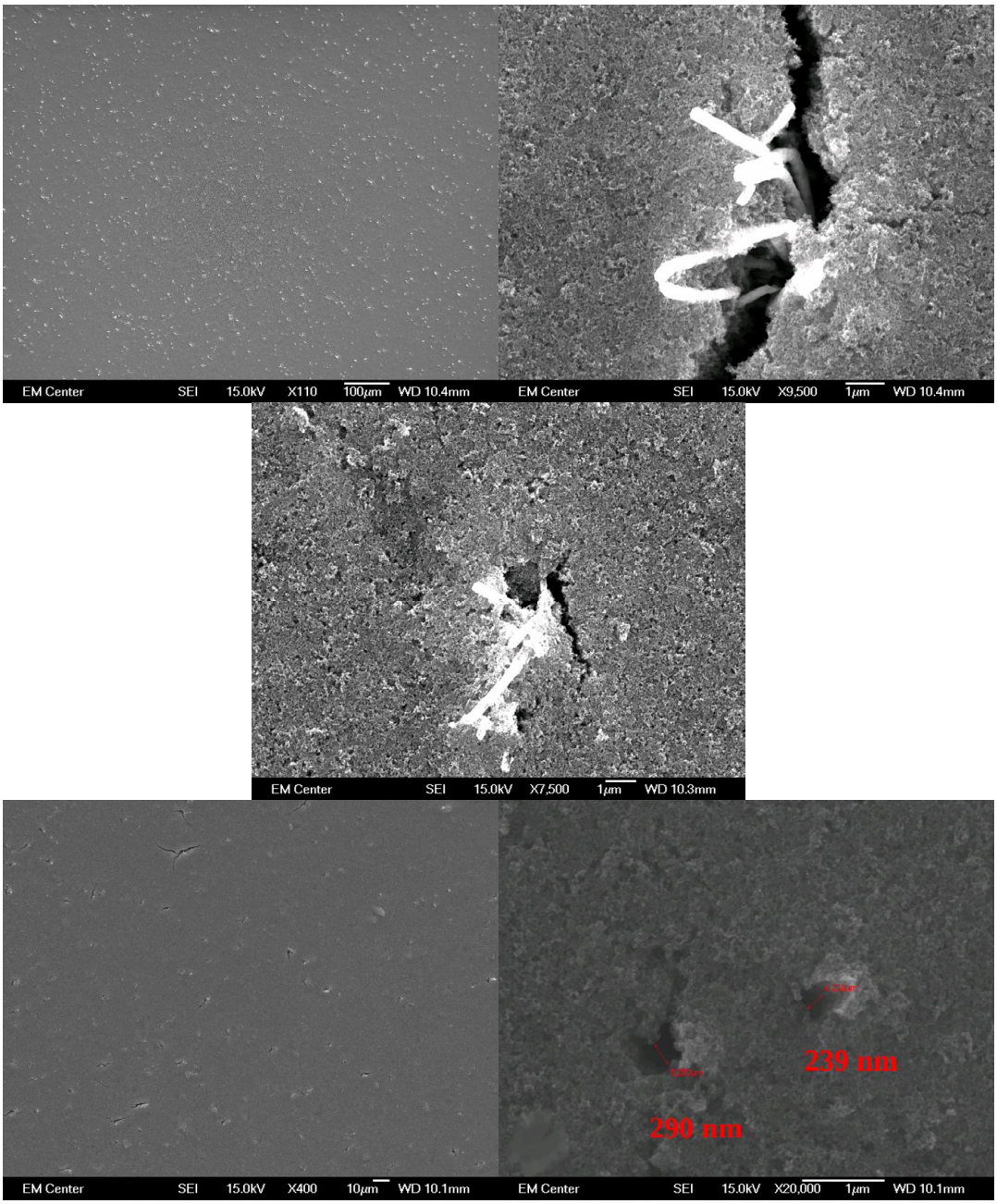

Figure 2.16: SEM images of nickel nanowire containing TiO_2 slurry before and after nanowire removal. The top three images are of the films with nickel nanowires still incorporated. The bottom two are after removal of the nickel nanowires in the acid bath.

After the nickel nanowires were removed from the films, the samples were dyed and digital images were taken to show the uniformity of the dye. The digital images in Figure 17 indicate that the majority of the samples are dyed in a fairly uniform manner; however, the darkness of the dyed samples varies which may again be a result of varied film thickness.

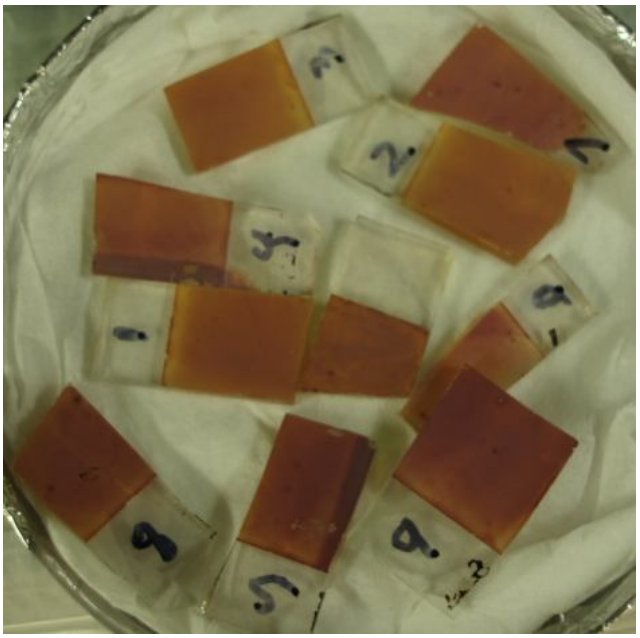

Figure 2.17: Digital images of dyed films after the removal of the nickel nanowires from the TiO_2 films. All samples have had the nickel nanowires removed except the unlabeled sample (center of image). The samples are labeled 1-9.

The current transients for the "nickel films" (refer to the Experimental) all show a significantly reduced if not completely eliminated current spike when the films are ≥ 6 μm thick, as determined by profilometry. Comparing the nickel films with the previous films of smooth and cracked the steady state currents on the current transients all wind up close to the same current with the current spike reduced or eliminated on the nickel and cracked film as shown in Figure 2.18.

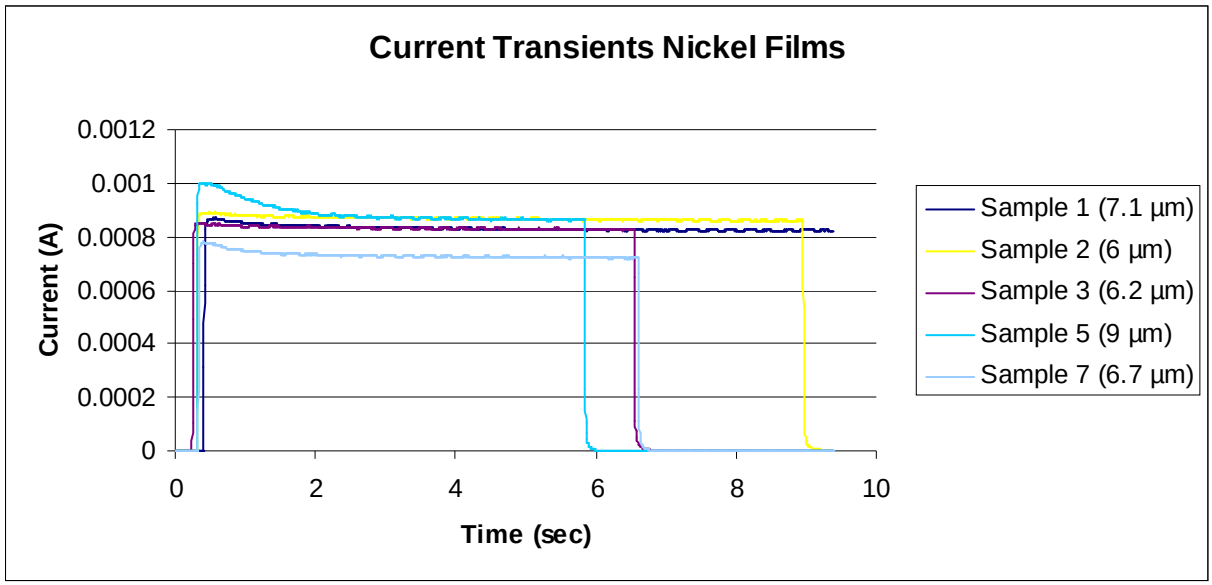

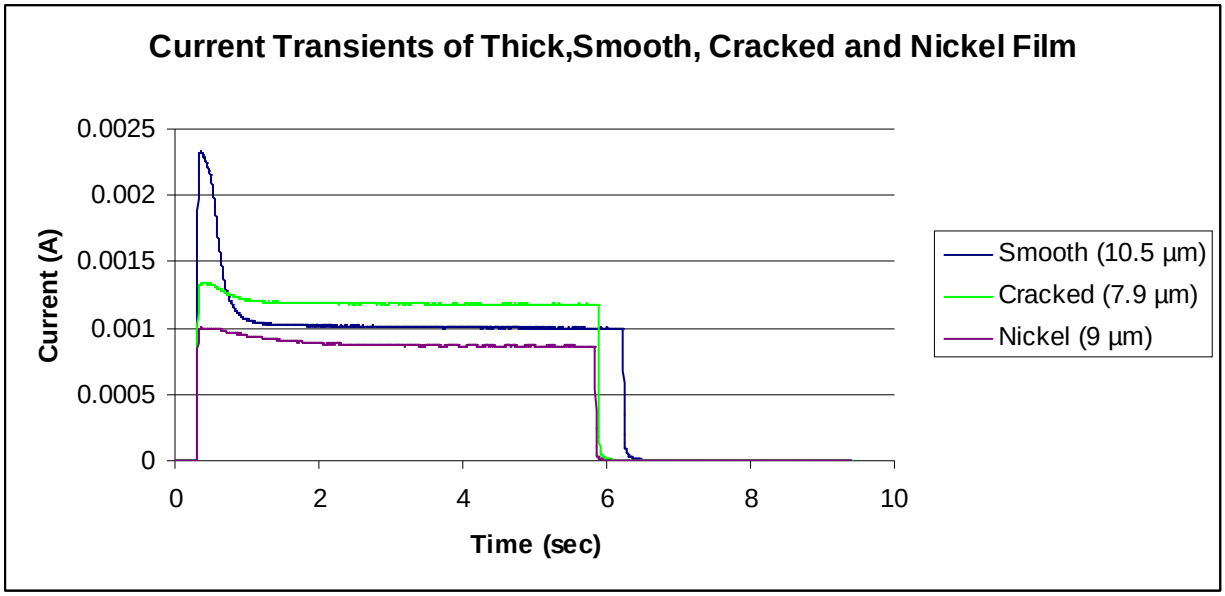

Figure 2.18: Current transients of the nickel nanowire films. Top graph is the current transients of the films 6 µm or greater. Bottom graph is a comparison of representative data from smooth, cracked, and nickel films.

The incident photon to current efficiencies (IPCEs) for the films, smooth, cracked and nickel removed, were qualitatively similar. However, as with the comparison between the smooth and the cracked films the IPCE % overall are lower in the nickel films indicating possibility a slow electron injection rate into the anode. Again this maybe due to less TiO_2 which leads to less of dye and thus fewer electrons generated. However, the SEM images of the films

would suggest that the nickel films would have more TiO_2 than the cracked. When looking at the dyed films directly the nickel films do appear to have a lighter purple tint then the other films, which indicate that there is less dye; however, as P25 is opaque UV absorption measurements are unable to be obtained to determine the dye concentration.

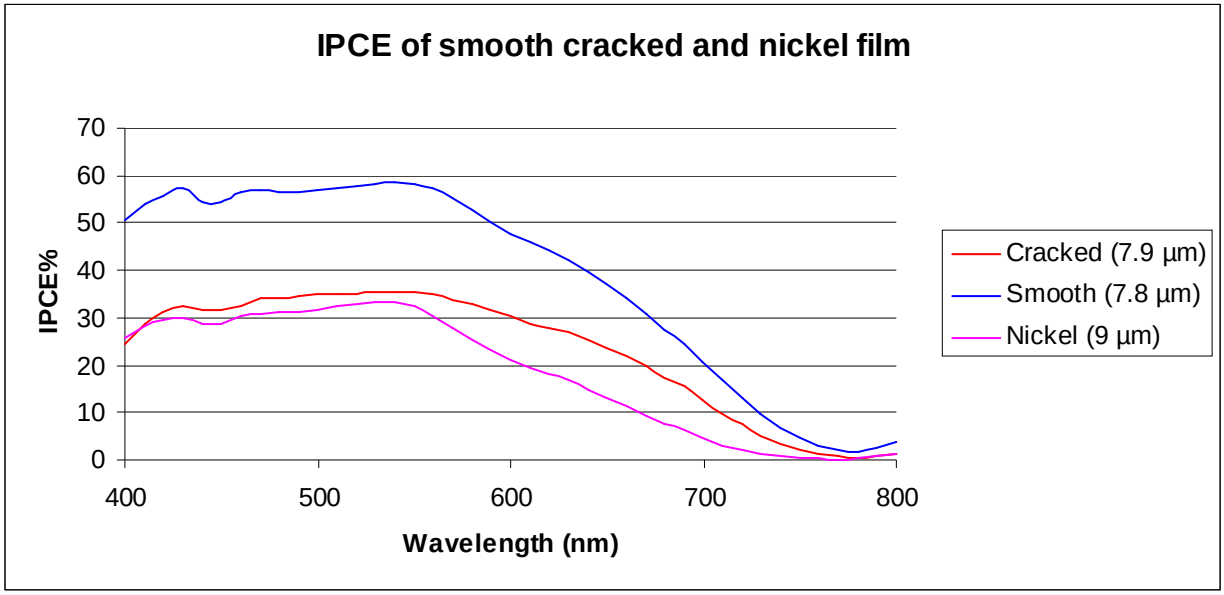

Figure 2.19: IPCE of smooth cracked and nickel films.

The voltage transients are similar for the smooth, cracked and nickel films as well with a steady state voltage at 0.5 V and decays to zero in 4-5 seconds. The IPCE and voltage transients indicate that the cells are functioning similar to one another supporting the direct comparison. The current versus potential scans are also similar, with V_{oc} values in the range of ~0.5 V. However, the J_{sc} values in the nickel films are 0.0002 A less than for the smooth and cracked films. This may be due to the films being slightly thinner, thus not having as much dye to produce electrons reducing the current. However, with the comparison of the IPCEs with the thicker nickel film and the lighter color of the films themselves the lack of dye maybe caused by the dye not bonding correctly to the TiO_2 rather then missing TiO_2. It is also noteworthy that the fill factor (FF) of the nickel film is 0.535 verses 0.616 and 0.650 for the smooth and the cracked

films respectively, this clearly indicates that the nickel films are performing more poorly then the other two films.

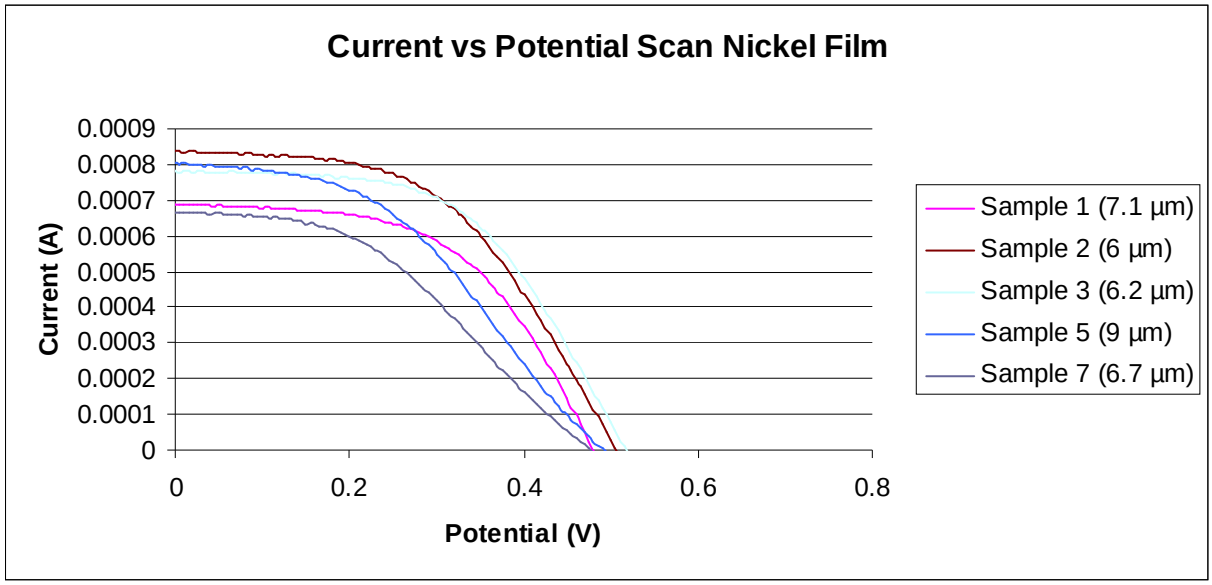

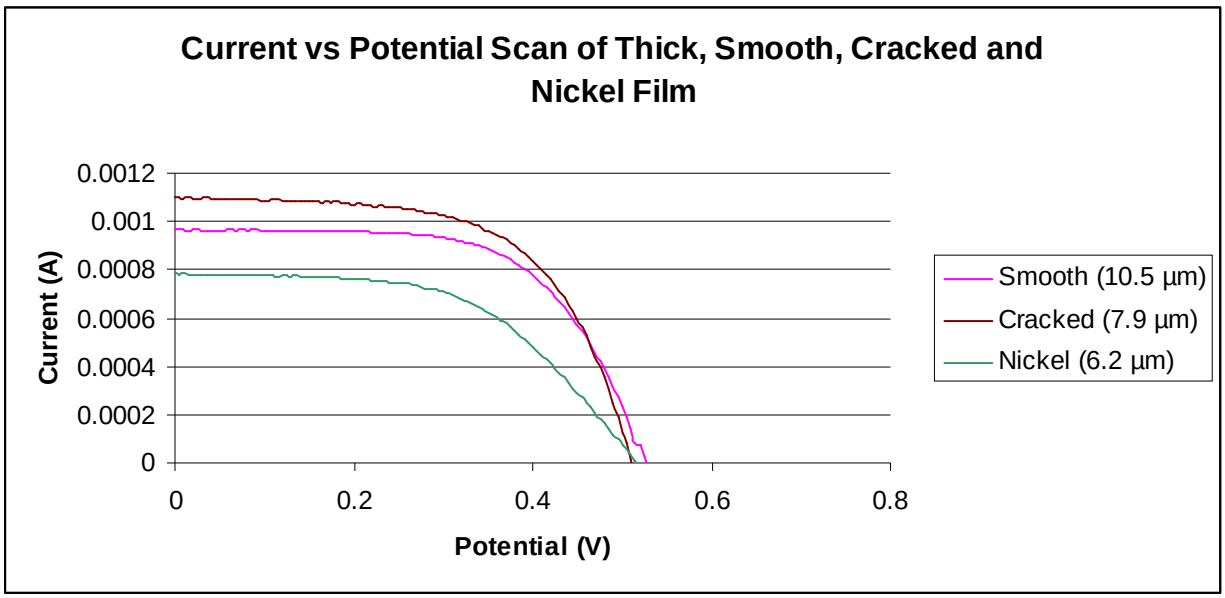

Figure 2.20: Current vs. potential scans of DSSCs that use TiO_2 films with void space created by aligned nickel nanowires.

Although the nickel nanowire/void space films have some differences from the smooth/cracked TiO_2 films, the overall trend appears to have some promising aspects with regard to removing cobalt mediator diffusion as the rate limiting step for DSSCs. However, there are

many questions regarding the current sets of data that will need to be answered before this hypothesis of introducing void space to remove diffusion limiting aspects in DSSCs can be proved or disproved.

Conclusion:

In conclusion, the concept of introducing void space into TiO_2 films via removable nanoparticles is promising as a possible way of increasing the rate of cobalt mediator transport in DSSCs. Although efforts to incorporate polystyrene nanoparticles, magnetite nanoparticles, and iron nanowires to introduce void space all had various associated problems, each of these approaches lead to important information about this system and resulted in the conclusion: mesoporous TiO_2 films incorporating other particles can be formed and the particles later removed; however, the synthesis and removal of nanoparticles is complicated when the particles are ferromagnetic and easy to oxidize.

The preliminary work done in this paper on the introduction of void space by the incorporation and subsequent removal of magnetically aligned nickel nanowires is promising. The current transient data obtained on this system supports the hypothesis that introducing channels of void space into the TiO_2 may reduce the mass transport limitation of cobalt mediators in DSSCs. This was shown through the reduced current spike in the nickel and cracked films compared to the smooth films. However, with the small sample size and some variances in the films themselves, further work is needed to confirm these findings. The major issues that need to be addressed are film thickness, uniformity of the P25 slurry, film uniformity, nanowires dispersion, and of course more data and testing is needed to fully understand the reduction of the current spike. Some of the solutions to these issues and answers to these questions could be

determined by using thicker films, making P25 slurries on a large scale to remove the small difference that can occur through evaporation, rotating the magnetic field to allow the film to lay flat with gravity as it dries and limiting the nanowires length to 10-20 μm to allow for easy dispersion and alignment. Also further testing is needed to determine why the steady state current stays relatively the same as it would be expected to increase as you increase mass transport. Determining the amount of dye absorbed onto the TiO_2 may help determine if the electron injection to the anode has become the limiting rate, which would explain the steady state staying the same. Also determining the amount of dye adsorbed onto the nickel films may display a problem with the dye may have bonding to these particular films. However, this may not ultimately be the problem as the majority of the nickel films in this study are thinner then the other films. Finally, these experiments need to be repeated multiple times to confirm the findings because of significant variability in film quality, thickness, ect...

REFERENCES:

1) Grätzel, M. *Nature* **2001**, *414*, 338-346.
2) Lewis, N. S.; Nocera, D. G. *PNAS* **2006**, *103*, 15729-15735.; Ginley, D. et al. *MRS Bulletin*, **2008**,*33*, 355-364.
3) Feeley, III,T.J.; Murphy, J.; Hoffmann, J.; Renninger, S.A. Executive Summary. A Review of DOE/NETL's Mercury Control Technology R&D Program for Coal-Fired Power Plants; U.S. Department of Energy, National Energy Technology Laboratory Science Applications International Corporation: Washington DC, 2003; 1.
4) Conti, J.; Holtberg, P; Landstrom, P; ect. Greenhouse gas emissions overview. *Emissions of Greenhouse Gases in the United States 2009*; U.S Energy Information Administration: Washington DC, 2011; 1-2.
5) Green, M.A.; Emery, K.; Hishikawa, Y.; Warta, W.; Dunlop, E.D. *Prog. Photovolt: Res. Appl.* **2012**, *20*, 12-20.
6) Cazzanti, S.; Caramori, S.; Argazzi, R.; Elliot,C.M.; Bignozzi,C.A. *J. Am. Chem. Soc.* **2006**, *128*, 9996-9997.
7) Nelson, J.J.; Amick, T.J.; Elliott, C.M. *J. Phys. Chem. C* **2008**, *112*, 18255-18263.
8) Feldt, S.M.; Gibson, E.A.; Gabrielesson, E.; Sun,L.; Boschloo, G.; Hagfeldt, A. *J. Am. Chem. Soc.* **2010**, *132*, 16714-16724.
9) Phadke, S.; Stanley, J. B.; Sorge, J. D.; Birnie III, D.P. *Journal of SID* **2007**, *15*, 1084-1093.
10) Qi, L.; Birnie III, D.P. *Materials Letters*, **2007**, *61*, 2191-2194.
11) Phadke, S.; Ho, J.; Birnie III, D. P. *Materials Letters*, **2009**, *63*, 2619-2621.
12) Ye, X. R.; Daraio, C.; Talbot, J. B. ; Jin, S. *J. Nanosci. Nanotechnol*. **2006**, 6, 852-856.
13) Sahoo, Y.; Goodarzi, A.; Swihart, M.T.; Ohulchanskyy, T.Y.; Kaur, N.; Furlani, E. P.; Prasad, P. N. **J. Phys. Chem. B 2005**, *109*, 3879-3885.
14) Nishio, K.; Ikeda, M.; Gokon, N.; Tsubouchi, S.; Narimatsu, H.; Mochizuky, Y.; Sakamoto, S.; Sandhu, S.; Abe, M.; Handa, H. *Journal of Magnetism and Magnetic Materials* **2007**, *310*, 2408-2410.
15) Lim, J.-H.; Chae, W.-S.; Lee, H.-O.; Malkinski, L.; Min, S.-G.; Wiley, J. B.; Jun, J.-H.; Lee, S.-H.; Jung, J.-S. *J. Appl. Phys.* **2010**, *107*,:09A334.
16) Haehnel, V.; Fahler, S.; Schaaf, P.; Miglierini, M.; Mickel, C.; Schultz, L.; Schorb, H. *Acta. Materialia*, **2010**, *58*, 2330-2337.
17) Bentley, A.K.; Farhoud, M.; Ellis, A.B. *J. Chem. Edu*. **2005**, *82*, 765-768.
18) Neto, C.; Joseph, K. R.; Brant, W. R. *Phys. Chem. Chem. Phys.* **2009**, *11*, 9537-9544.
19) Arabatzis, I.M.; Antonaraki, S.; Stergiopoulos, T.; Hiskia, A.; Papaconstantinou, E.; Bernard, M.C. ; Falaras, P. *Journal of Photochemistry and Photobiology A : Chemistry* **2002**, *149*, 237-245.
20) Smestad, Greg P.; Grätzel, Michael *J. Chem. Ed.* **1998**, 75, 752-757.